Development of mixed-phase clouds from multiple aerosol size distributions and the effect of the clouds on aerosol removal

Mark Z. Jacobson

Department of Civil and Environmental Engineering, Stanford University, Stanford, California, USA

Received 22 June 2002; revised 6 November 2002; accepted 14 January 2003; published 23 April 2003.

[1] This paper provides numerics for cloud and precipitation development from multiple aerosol size distributions and examines the effect of clouds and precipitation on aerosol removal. Numerical techniques are given for (1) simultaneous liquid and ice growth onto multiple aerosol size distributions, (2) diffusiophoretic, thermophoretic, gravitational, etc., coagulation among liquid, ice, and graupel, and their aerosol components, (3) contact freezing (CF) of drops by size-resolved interstitial aerosols, (4) heterogeneous plus homogeneous freezing, (5) liquid drop breakup, (6) coagulation of cloud hydrometeors and incorporated aerosols with interstitial aerosols, (7) coagulation of precipitation hydrometeors with interstitial and below-cloud aerosols (washout), (8) removal of precipitation and incorporated aerosols (rainout), (9) below-cloud evaporation/sublimation to smaller hydrometeors and aerosol cores, (10) gas washout, and (11) aqueous chemistry. Major conclusions are (1) hydrometeor-hydrometeor coagulation appears to play a substantial role in controlling aerosol-particle number globally, (2) washout (aerosol-hydrometeor coagulation) may be a more important in-plus below-cloud removal mechanism of aerosol number than rainout (the opposite is true for aerosol mass), (3) close-in diameter dual peaks in observed cloud distributions may be in part due to different activation characteristics of different aerosol distributions, (4) evaporative cooling at liquid drop surfaces in subsaturated air may be a mechanism of drop freezing (termed ''evaporative freezing'' here), and (5) heterogeneous-homogeneous freezing may freeze more upper-tropospheric drops than CF, but neither appears to affect warm-cloud hydrometeor distributions or aerosol scavenging substantially. *INDEX TERMS:* 0305 Atmospheric Composition and Structure: Aerosols and particles (0345, 4801); 0320 Atmospheric Composition and Structure: Cloud physics and chemistry; 0322 Atmospheric Composition and Structure: Constituent sources and sinks; 0345 Atmospheric Composition and Structure: Pollution—urban and regional (0305); 0365 Atmospheric Composition and Structure: Troposphere—composition and chemistry; *KEYWORDS:* cloud microphysics, aerosol-cloud interactions, coagulation, freezing, condensation, evaporation

Citation: Jacobson, M. Z., Development of mixed-phase clouds from multiple aerosol size distributions and the effect of the clouds on aerosol removal, *J. Geophys. Res.*, *108*(D8), 4245, doi:10.1029/2002JD002691, 2003.

1. Introduction

[2] Since the 1950s, many models treating size-resolved microphysics and/or microphysics coupled with chemistry have been developed to study individual clouds or multi-cloud storms [e.g., *Mordy*, 1959; *Danielsen et al.*, 1972; *Hall*, 1980; *Flossmann et al.*, 1985; *Kogan*, 1991; *Lee*, 1992; *Chen and Lamb*, 1994, 1999; *Tzivion et al.*, 1994; *Ackerman et al.*, 1995; *Reisin et al.*, 1996; *Guriciullo and Pandis*, 1997; *Feingold et al.*, 1996, 1998; *Liu and Seidl*, 1998; *Zhang et al.*, 1999; *Ovtchinnikov and Kogan*, 2000]. Due to heavier computational burden, global and limited area three-dimensional weather, climate, and cloud-chemistry models have generally treated cloud liquid and ice as bulk parameters [e.g., *Manabe and Holloway*, 1971; *Kuo*, 1974; *Arakawa and Schubert*, 1974; *Sundqvist*, 1978; *Hegg et al.*, 1984, 1989; *Betts and Miller*, 1986; *Slingo*, 1987; *Grell et al.*, 1991; *Barth et al.*, 1992, 2001; *Tiedtke*, 1993; *Wang and Chang*, 1993; *Lee and Park*, 1994; *Ferrier*, 1994; *Walko et al.*, 1995; *Xu and Randall*, 1996; *Wang*, 1996; *Fowler et al.*, 1996; *Taylor et al.*, 1997; *Sud and Walker*, 1999; *Ding and Randall*, 1998].

[3] Similarly, due to computational burden, all models of global-scale indirect forcing of aerosols to date have treated cloud water and ice as bulk parameters spread over cloud condensation nuclei (CCN) and/or ice deposition nuclei (IDN) distribution determined empirically from the predicted background aerosol distribution [e.g., *Boucher and Lohmann*, 1995; *Chuang and Penner*, 1995; *Kogan et al.*, 1997; *Rotstayn and Penner*, 2001; *Ghan et al.*, 2001; *Lohmann et al.*, 2000; *Jones et al.*, 2001; *Lohmann*, 2002; *Menon et al.*, 2002]. To date, three-dimensional global-scale models of climate, weather, cloud chemistry, air pollution, and aerosol feedbacks to climate have not simulated (1) size-resolved simultaneous condensational and depositional

0148-0227/03/2002JD002691$09.00

growth of aerosol particles to form cloud liquid and/or ice, (2) coagulation among size-resolved cloud liquid and/or ice together with their aerosol components to form larger liquid, ice, and graupel, (3) contact freezing (CF) by size-resolved aerosols with size-resolved hydrometeors, (4) coagulation of interstitial size-resolved aerosols and their components with the size-resolved liquid, ice, and graupel, (5) below-cloud size-resolved evaporation or melting of falling hydrometeors, (6) below-cloud coagulation of size-resolved hydrometeors with aerosols, and (7) treatment of charge, diffusiophoresis, and thermophoresis in coagulation interactions.

[4] The purpose of this paper is to provide the numerics for and an analysis of these and other cloud processes. The equations described are intended for use in a one-dimensional gas-aerosol-cloud module that fits into a three-dimensional model already containing a cumulus and stratus bulk parameterization of clouds. The algorithms described can also be used in a model that simulates the thermodynamic development of individual clouds at high spatial and temporal resolution, although examples of this application are not given here. The module is intended to simulate treatment of cloud formation, conversion, and decay, precipitation, aerosol-cloud interactions, aerosol wet removal (rainout and washout), gas wet removal (washout), and cloud chemistry. All processes described conserve energy and the masses of water, aerosols, and gases exactly. All processes are stable and positive definite, regardless of the time step, and are, with three exceptions (hydrometeor surface temperature, large-scale precipitation, and aqueous chemistry), noniterative. In operator-split regional and global models, the time interval for cloud processes is often 15–60 min, so the use of noniterative schemes stable over any time step is advantageous. To date, the module has been implemented in each column of a model [*Jacobson*, 2001, 2002a, 2002b] that nests from the global through urban scales. Predictions of zonally averaged cloud fraction, cloud liquid water, and precipitation from a global version of the model containing most of the algorithms described here have been compared with climatalogical fields and data [*Jacobson*, 2002a].

2. Summary of Processes

[5] The order of processes treated is summarized as follows: section 3, acquisition of parameters for aerosol-cloud processes; section 3.1, subgrid cumulus cloud parameters; section 3.2, cumulus convection of gases and aerosols; section 3.3, stratus cloud parameters; section 3.4, vaporization of hydrometeor water from cumulus and stratus parameterizations; section 4, aerosol-cloud processes; section 4.1, water vapor condensational and depositional growth onto aerosols; section 4.2, partitioning from a moving to a fixed grid; section 4.3, hydrometeor settling from above and melting of hydrometeors from above; section 4.4, hydrometeor-hydrometeor coagulation; section 4.5, liquid drop breakup; section 4.6, contact freezing of liquid drops by aerosol particles; section 4.7, homogeneous and heterogeneous freezing of liquid drops; section 4.8, settling of hydrometeors and their aerosol components: aerosol rainout; section 4.9, aerosol-hydrometeor coagulation: aerosol washout; section 4.10, below-cloud hydrometeor evaporation/sublimation and evaporative freezing; section 4.11, evaporation of leftover hydrometeors to aerosol cores, large-scale precipitation; section 4.12, gas-hydrometeor dissolution: gas washout; section 4.13, aqueous chemistry.

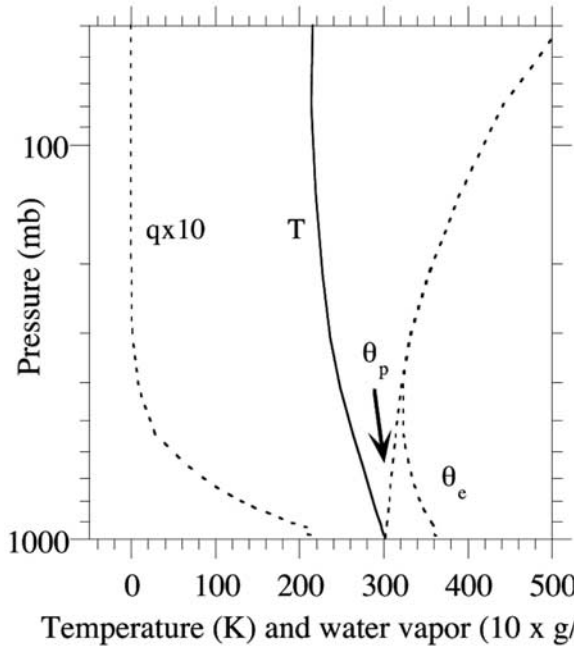

Figure 1. Initial ambient temperature (T), potential temperature (θ_p), equivalent potential temperature (θ_e), and water vapor (q) profiles for the one-dimensional simulation.

[6] Processes in section 3 are solved in all layers simultaneously. Processes in section 4 are solved in order from the top of the highest cloud layer to the surface, allowing the multiple processes treated in each layer to impact the hydrometeor distribution below. For some processes, the order of calculation follows naturally (e.g., condensation in the current layer and settling/melting of hydrometeors from above should precede coagulation in the current layer, which should precede breakup, which should precede settling to below, which should precede subcloud evaporation). For other processes, the order is somewhat arbitrary (e.g., CF, homogeneous/heterogeneous freezing, aerosol-hydrometeor coagulation can be treated in different order). Section 5.2 discusses some sensitivities to order.

[7] Several techniques described subsequently are analyzed in the context of a one-dimension simulation in which a cumulus parameterization is used to generate first guesses of subgrid clouds. Figure 1 shows the atmospheric conditions for the case. The atmospheric profile is unstable near the surface, suggesting that clouds of vertical extent can form. In the simulation, a cloud forms on top of 16 aerosol distributions, including externally mixed sea spray, soil, ammonium sulfate, black carbon (BC < 5% shell), organic matter (OM), all binary combinations of these five components (spray-soil, spray-sulfate, spray-BC, spray-OM, soil-sulfate, soil-BC, soil-OM, sulfate-BC, sulfate-OM, BC-OM), and a well-mixed internal mixture for all higher mixtures. These are the same distribution types as the 18 described by *Jacobson* [2002b], except the two distributions treated there (BC 5–20% shell and BC > 20% shell) that are ignored here for simplicity. For the distributions containing ions (all those

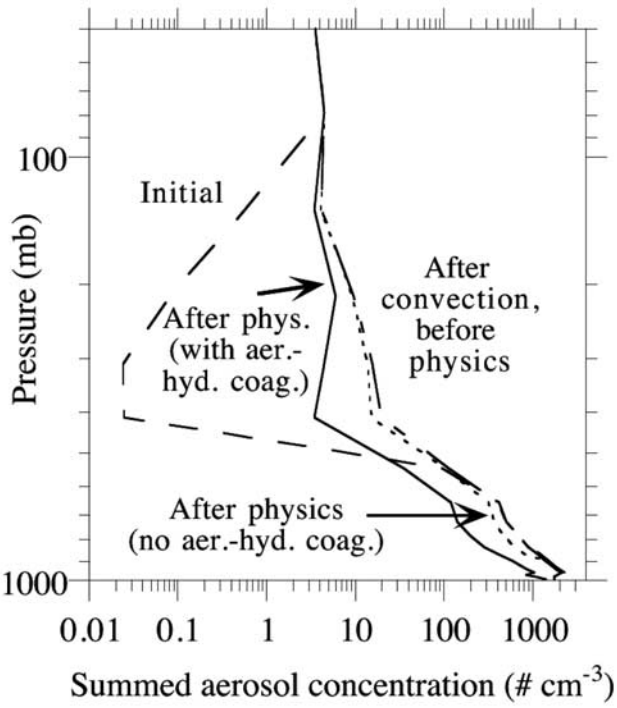

Figure 2. Weighted-average clear plus cloudy-sky aerosol concentration profiles, summed over all 16 aerosol size distributions treated, for the one-dimensional simulation. The figure shows the initial profile for clear and cloudy regions, the weighted-average clear- plus cloudy-sky profile after cumulus convective mixing but before microphysical calculations, and the weighted-average profile after all microphysical calculations. In one microphysical case, hydrometeor coagulation with interstitial and below-cloud aerosols was treated (with aer.-hyd. coag.); in the other, it was not (no aer.-hyd. coag.).

with sea spray and sulfate in them), water content was determined with an equilibrium hydration calculation at the ambient relative humidity of the layer prior to cloud formation. Figure 2 shows the initial aerosol number concentration profile, summed over all distributions. Figure 3 shows each initial distribution at 872 mb. The concentrations represent moderately polluted conditions.

3. Acquisition of Parameters for Aerosol-Cloud Processes

[8] The aerosol-cloud algorithms described here require preliminary steps to generate water vapor and aerosol profiles. These steps are described in the following sections.

3.1. Subgrid Cumulus Cloud Parameters

[9] The first step is to diagnose subgrid cumulus cloud fractions and mass fluxes and first guesses to cloud bulk water, precipitation, temperature, water vapor, and momentum for each subgrid cloud. When the grid spacing exceeds 10–15 km, this is done here with a cumulus parameterization that accounts for multiple subgrid clouds. For finer grid spacing, it is more physical to use a single-cloud module because the cumulus parameterization assumes that clouds do not fill an entire grid cell (to allow large-scale downflow to compensate for in-cloud upflow). A single-cloud module, though, becomes unphysical for scales >10–15 km since, on these scales, multiple clouds may exist. The cumulus parameterization used here is a modified Arakawa-Schubert algorithm [*Ding and Randall*, 1998], which accounts for downdrafts and predicts cumulus precipitation, bulk liquid water, bulk ice, cumulus fraction, and adjustments to large-scale temperature, momentum, and water vapor for each subgrid cloud. The vertical mass flux in each subgrid cloud is a function of the entrainment/detrainment rate, stability, and moist static energy in the cloud. The total vertical mass flux integrated over all subgrid clouds is balanced by large-scale subsidence. In a column with 23 tropospheric layers, nearly 500 subgrid cumulus clouds can form, each defined by a unique cloud base and top (22 bases and 22 tops are possible). The product of each subgrid cloud parameter and subgrid cloud fraction is summed over all subgrid clouds to give bulk values for each grid cell.

3.2. Cumulus Convection of Gases and Aerosols

[10] The second step is to mix convectively gases and aerosol particles in each subgrid cumulus cloud. This is done with a free-convective plume model, developed here from the boundary-layer plume model by *Lu and Turco* [1994]. The model convects gases and aerosols between each subgrid cumulus subcloud layer and cloud top. Although the numerical scheme for the plume model differs from that of the convective mass flux scheme used to transport water vapor and energy, gases and aerosols are mixed between the exact same levels in both cases. Because aerosols and cloud water are transported between the same layers, aerosol activation following water evaporation/sublimation from the cumulus parameterization is consistent with aerosol activation in a rising plume since the number of aerosols and mass of water are similar in both cases. The resulting vertical gas and aerosol distribution in each subgrid cloud is multiplied by the fraction of the subgrid cloud to obtain a weighted-average cloudy-sky vertical gas and aerosol distribution in each grid cell. Figure 2 shows how the module mixed a portion of the initial lower tropospheric aerosol profile to the middle and upper troposphere, where the initial aerosol distribution was low, in the one-dimensional case study. The plume model conserves mass and number exactly; so the gain in aerosols in the middle and upper troposphere in the figure was compensated for by an equivalent reduction in lower-tropospheric aerosols.

3.3. Stratus Cloud Parameters

[11] The third step is to predict stratus cloud fraction and bulk liquid water (adjusting temperatures in the process). This is done here with the scheme of *Mellor and Yamada* [1982], which predicts cloud fraction and bulk liquid water in each layer given turbulence terms and vertical gradients of energy and moisture. The total cloud fraction in a layer is the sum of stratus plus cumulus cloud fractions in the layer, limited by unity.

3.4. Vaporization of Hydrometeor Water From Cumulus and Stratus Parameterizations

[12] The fourth step is to evaporate/sublimate all in-cloud and precipitated bulk water from the cumulus and stratus

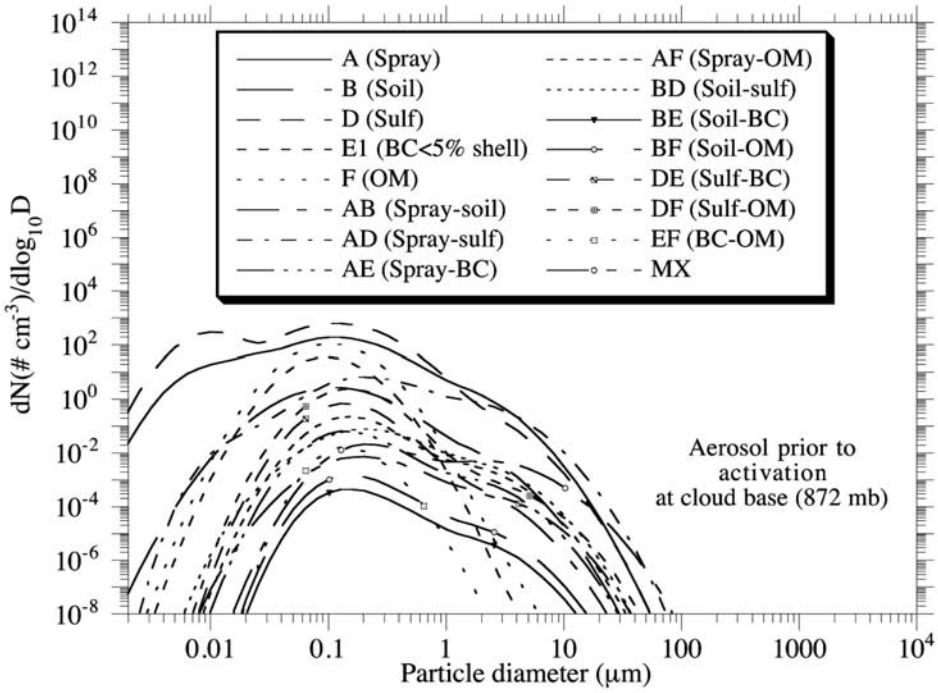

Figure 3. Initial distributions at 872 mb for each of the 16 aerosol types treated in the one-dimensional simulation. The letters identify the distribution.

calculations in each layer and readjust temperatures accordingly. This step is necessary to allow subsequent condensation and deposition onto size-distributed aerosols since the cumulus and stratus parameterizations produce bulk liquid and ice water only without consideration for their size distributions.

4. Aerosol-Cloud Processes

[13] Remaining steps are solved in order from the top of the highest cloud layer, found in section 3, to the surface.

4.1. Water Vapor Condensational and Depositional Growth Onto Aerosols

[14] In this step, water vapor evaporated/sublimated during the third step in section 3.4. is recondensed/redeposited onto aerosol particles. The scheme developed here has the following properties: it is (1) noniterative and unconditionally stable for any time step, (2) positive definite for any time step, (3) exactly conserves water mass and energy between the gas phase and all size bins of all hydrometeor distributions, (4) exactly conserves aerosol and hydrometeor particle number, (5) solves condensational and ice depositional growth equations simultaneously, accounting for different vapor pressures over different sizes, and (6) solves condensation and deposition over any number of hydrometeor distributions simultaneously. Previous cloud growth schemes are numerous [e.g., *Mordy*, 1959; *Hall*, 1980; *Flossmann et al.*, 1985; *Tzivion et al.*, 1989; *Kogan*, 1991; *Chen and Lamb*, 1994]. Whereas most schemes exhibit some of the properties listed, none captures all properties simultaneously.

[15] The numerical treatment assumes that aerosol particles can be described by any number of size distributions (N_T), each with any number of size bins (N_B) and any number of components within each size bin. Each size bin i in each size distribution $N = 1$, N_T is characterized by a number concentration, n_{Ni} (number of particles per cubic centimeter of air). Each component q in each size bin of each distribution is characterized by a mole concentration, $c_{q,Ni}$ (mol cm^{-3} of air). In the example case described here, $N_T = 16$, where the size distributions treated are shown in Figure 3.

[16] The volume of one particle is calculated assuming a particle contains a solution and nonsolution component, and solution density varies with electrolyte concentration. Single-particle volumes (cm^3 per particle) are $\upsilon_{Ni} = v_{Ni}/n_{Ni}$, where

$$v_{Ni} = v_{s,Ni} + \sum_{q=1}^{N_{NS}} v_{q,Ni} \tag{1}$$

is the volume concentration (cm^3 of particle per cm^3 of air) of the total particle: $v_{s,Ni}$ is the volume concentration of the solution, N_{NS} is the number of nonsolution components, $v_{q,Ni} = m_q c_{q,Ni}/\rho_q$ is the volume concentration of each nonsolution component, m_q is the molecular weight (g mol^{-1}) of component q, and ρ_q is the mass density (g cm^{-3} of component) of component q. The volume concentration of a solution is calculated as $v_{s,Ni} = \boldsymbol{m}_{s,Ni}/\rho_{s,Ni}$, where

$$\boldsymbol{m}_{s,Ni} = m_w c_{w,Ni} + \sum_{q=1}^{N_S} m_q c_{q,Ni} \tag{2}$$

is the mass concentration (g cm^{-3} of air) of the solution (m_w is the molecular weight of water, $c_{w,Ni}$ is the mole concentration of hydrated liquid water at sub-100% relative

humidity, N_S is the number of electrolytes in the solution), and

$$\rho_{s,Ni} = \left[\sum_{q=1}^{N_E} \frac{\chi_{q,Ni}}{\rho_{a,q,Ni}}\right]^{-1} \tag{3}$$

is the mass density (g cm^{-3} of solution) of the solution, where $\chi_{q,Ni} = m_q c_{q,Ni}/\boldsymbol{m}_{s,Ni}$ is the mass fraction of component q in solution and $\rho_{a,q,Ni}$ is the mass density of electrolyte q as if it were alone in solution at the same weight percent as the current weight percent of total solute [e.g., *Tang*, 1997].

[17] Each size bin in each size distribution is characterized by a high- and low-edge volume, each of which equals a constant, $V_{\rm rat}$, multiplied by the high- and low-edge volume, respectively, of the next smallest bin. All particles in the bin have a single characteristic volume (υ_{Ni}) between the low- and high-edge volumes of the bin. This single volume can change as the particles grow, evaporate, coagulate, etc. If the volume increases above the high-edge volume of the bin, all particles in the bin are moved to and averaged with particles in the next largest bin. This size-bin structure is the "moving-center" structure [*Jacobson*, 1997a, 1999, pp. 420–421].

[18] The ordinary differential equations for water vapor condensation/evaporation (equation (4)) and deposition/sublimation (equation (5)) onto multiple aerosol distributions, and the corresponding vapor-hydrometeor mass balance equation (equation (6)) are

$$\frac{dc_{L,Ni,t}}{dt} = k_{L,Ni,t-h}\left(C_{v,t} - S'_{L,Ni,t-h}C_{s,L,t-h}\right), \tag{4}$$

$$\frac{dc_{I,Ni,t}}{dt} = k_{I,Ni,t-h}\left(C_{v,t} - S'_{I,Ni,t-h}C_{s,I,t-h}\right), \tag{5}$$

$$\frac{dC_{v,t}}{dt} = -\sum_{N=1}^{N_T}\sum_{i=1}^{N_B}\left[k_{L,Ni,t-h}\left(C_{v,t} - S'_{L,Ni,t-h}C_{s,L,t-h}\right) + k_{I,Ni,t-h} \cdot\left(C_{v,t} - S'_{I,Ni,t-h}C_{s,I,t-h}\right)\right], \tag{6}$$

where t and $t-h$ indicate the end and beginning, respectively, of a time step of h seconds, L and I indicate liquid and ice, respectively, N and i indicate the aerosol distribution and size bin in the distribution, respectively, from which the hydrometeor originates, N_T and N_B are the number of aerosol size distributions and size bins, respectively, in each aerosol distribution, c_L and c_I indicate liquid or ice mole concentration (mol cm^{-3} of air) resulting from condensation and deposition, respectively, C_v indicates a water vapor mole concentration, C_s is a saturation vapor mole concentration over a flat, dilute liquid water or ice surface, S' is the saturation ratio at equilibrium of water vapor over a liquid solution or ice surface, and k_L and k_I are the respective growth rates (s^{-1}) of water vapor to a liquid- and ice-covered aerosol particle surface. Note that c_L differs from c_w in that the former is liquid water due to nonequilibrium condensation and the latter is liquid water due to aerosol-equilibrium hydration.

[19] The saturation ratios at equilibrium are calculated from Köhler theory assuming the Kelvin and solute effects affect the saturation ratio at equilibrium over liquid water, whereas only the Kelvin effect affects that over ice. Thus

$$S'_{L,Ni,t-h} \approx 1 + \frac{2\sigma_{L,Ni,t-h}m_w}{r_{Ni,t-h}R^*T\rho_L} - \frac{3m_w}{4\pi r^3_{Ni,t-h}\rho_L n_{Ni,t-h}}\sum_{q=1}^{N_s} c_{q,Ni,t-h}, \tag{7}$$

$$S'_{I,Ni,t-h} \approx 1 + \frac{2\sigma_{I,Ni,t-h}m_w}{r_{Ni,t-h}R^*T\rho_I}, \tag{8}$$

where σ is surface tension over liquid or ice, (g s^{-2}), m is molecular weight (g mol^{-1}), ρ is liquid or ice density (g cm^{-3}), r is radius (cm), R^* is the universal gas constant (8.3145×10^7 g cm^2 s^{-2} mol^{-1} K^{-1}), T is temperature (K), n is the number concentration of aerosol particles of size i in distribution N (particles cm^{-3}-air), and c_q is the mole concentration of soluble component q in aerosol particles of size i in distribution N. Soluble components include dissociated or undissociated electrolytes and undissociated soluble molecules. The surface tension used here for distributions containing water and soluble material is taken from the study of *Facchini et al.* [1999], who provide a relationship between surface tension and dissolved organic content. The form of the relationship is similar for inorganic material, as shown by *Li et al.* [1998]. For this study, the empirical relationship of *Facchini et al.* [1999] is used, but applied to both inorganic and organic solutes. For BC, the surface tension was assumed to be 60 mN m^{-1}, lower than that of pure graphite (68 mN m^{-1}) to account for a slight coating of organic material on combusted soot.

[20] Equation (7) can be rewritten as

$$S'_{L,Ni,t-h} \approx 1 + \frac{a_{L,Ni,t-h}}{r_{Ni,t-h}} - \frac{b_{L,Ni,t-h}}{r^3_{Ni,t-h}} \tag{9}$$

$$a_{L,Ni,t-h} = \frac{2\sigma_{L,Ni,t-h}m_w}{R^*T\rho_L} \qquad b_{L,Ni,t-h} = \frac{3m_w}{4\pi\rho_L n_{Ni,t-h}}\sum_{q=1}^{N_s} c_{q,Ni,t-h}$$

The critical radius (cm) and critical supersaturation for cloud activation, derived from equation (9), are

$$r^*_{L,Ni,t-h} = \sqrt{\frac{3b_{L,Ni,t-h}}{a_{L,Ni,t-h}}} \text{ and } S^*_{L,Ni,t-h} = 1 + \sqrt{\frac{4a^3_{L,Ni,t-h}}{27b_{L,Ni,t-h}}}, \tag{10}$$

respectively. Above 0°C, no ice can form, and all particles in any size bin in the liquid distribution can serve as CCN. In this case, the number concentration of CCN in each bin is $n_{\rm lq,Ni} = n_{Ni}$ and the volume concentration of each solution and the mole concentration of each solution and nonsolution aerosol component in each bin of the liquid CCN distribution are $v_{s,\rm lq,Ni} = v_{s,Ni}$ and $c_{\rm lq,q,Ni} = c_{q,Ni}$, respectively. A CCN can activate into a liquid cloud drop when (1) $r_{Ni,t-h} > r^*_{L,Ni,t-h}$ and $C_{v,t-h} > S'_{L,Ni,t-h}C_{s,L,t-h}$ or (2) $r_{Ni,t-h} \le r^*_{L,Ni,t-h}$ and $C_{v,t-h} > S^*_{L,Ni,t-h}C_{s,L,t-h}$. For determining which aerosols activate (and to replicate as closely as possible conditions in a rising plume), $C_{v,t-h}$ in the criteria just given is limited to the smaller of the actual value of $C_{v,t-h}$ and the maximum value that one might

expect during adiabatic ascent in a cloud (which is given by *Kreidenweis et al.* [2003], for example). $C_{v,t-h}$ is not limited in any other equation.

[21] Below 0°C, condensation must compete with deposition to ice nuclei. At subfreezing temperatures, the saturation vapor mole concentration over ice is lesser than that over liquid, so ice growth is favored. Whereas any aerosol particle can serve as a CCN, only selected particle types can serve as IDN. Here it is assumed that the number concentration of IDN, the volume concentration of an IDN solution, and the mole concentrations of IDN solution and nonsolution aerosol components in a bin are $n_{\mathrm{ic},Ni} = F_{\mathrm{IDN},Ni} n_{Ni}$, $v_{s,\mathrm{ic},Ni} = F_{\mathrm{IDN},Ni} v_{s,Ni}$, and $c_{\mathrm{ic},q,Ni} = F_{\mathrm{IDN},Ni} c_{q,Ni}$, respectively, where

$$F_{\mathrm{IDN},Ni} = \sum_{q=1}^{N_S+N_{\mathrm{NS}}} P_{\mathrm{IDN},q,Ni} c_{q,Ni} \Bigg/ \sum_{q=1}^{N_S+N_{\mathrm{NS}}} c_{q,Ni} \tag{11}$$

is the fraction of aerosol particles in each bin in each distribution that can serve as IDN. In this equation, $P_{\mathrm{IDN},q,Ni}$ is the probability that a given component q in a particle can serve as an IDN. Probabilities are estimated from the work of *Pruppacher and Klett* [1997] who suggest that nonhygroscopic supermicron particles, soil components, a small fraction of OM, certain viruses and bacteria, and a small fraction of sea salt make the best ice nuclei. Soot is not a good ice nucleus, except below −15°C and at high supersaturations. Some pollutants deactivate ice nuclei. For this study, $P_{\mathrm{IDN}} = 0.05$ for BC when $T < -15$°C and 0 when $T > 15$°C, 0.15 for OM, 0.5 for soil, 0.01 for S(VI), 0.01 for H_2O, 0.2 for Na, 0.2 for Cl, 0.02 for other components, and 0 for particles <0.6 μm diameter. An IDN can activate to an ice crystal when $C_{v,t-h} > S'_{I,Ni,t-h} C_{s,I,t-h}$. If IDN activation occurs in a bin, the number concentration of CCN is limited by $n_{\mathrm{lq},Ni} = n_{Ni} - n_{\mathrm{ic},Ni}$. Liquid distribution aerosol components are also limited accordingly.

[22] Previous studies have generally parameterized the total number of IDN from an empirical equation such as by *Meyers et al.* [1992]. The reason such an equation for not being used here is that it does not separate the number of IDN by size and it predicts the same number of IDN at a given temperature, regardless of the atmospheric loading or aerosol composition. The methodology proposed here separates IDN by size and always predicts a quantity of IDN in a bin consistent with the aerosol loading and composition in the bin. However, much uncertainty exists in the values of P_{IDN}. Despite the difference in treatment, the range in total number concentration of IDN predicted in all levels of the column simulation here (0.7–24 l^{-1}) fell close to within the range of *Meyers et al.*'s [1992] parameterization (0.5–13 l^{-1}).

[23] For liquid and ice bins in which no activation occurs, the growth rates of particles, $k_{L,Ni}$ and $k_{I,Ni}$, are set to zero. The growth rates of activated CCN and IDN are calculated as [e.g., equations 17.62 and 17.53 of *Jacobson*, 1999],

$$k_{L,Ni} = \frac{n_{\mathrm{lq},Ni} 4\pi r_{Ni} D_v \omega_{v,L,Ni} F_{v,L,Ni}}{\dfrac{m_w D_v \omega_{v,L,Ni} F_{v,L,Ni} L_e S'_{L,Ni} C_{s,L}}{\kappa_m \omega_{h,Ni} F_{h,L,Ni} T} \left(\dfrac{L_e m_w}{R^* T} - 1 \right) + 1} \tag{12}$$

and

$$k_{I,Ni} = \frac{n_{\mathrm{ic},Ni} 4\pi r_{Ni} D_v \omega_{v,I,Ni} F_{v,I,Ni}}{\dfrac{m_w D_v \omega_{v,I,Ni} F_{v,I,Ni} L_s S'_{I,Ni} C_{s,I}}{\kappa_m \omega_{h,Ni} F_{h,I,Ni} T} \left(\dfrac{L_s m_w}{R^* T} - 1 \right) + 1}, \tag{13}$$

respectively, where all terms are evaluated at time $t - h$. In these equations, D_v is the diffusion coefficient of water vapor in air ($cm^2\ s^{-1}$), ω_v and ω_h are dimensionless factors for water vapor and energy, respectively, that account for corrections for collision geometry and sticking probability during growth, F_v and F_h are dimensionless ventilation coefficients for vapor and energy, respectively, L_e and L_s are latent heats of evaporation and sublimation, respectively ($J\ g^{-1}$), κ_m is the thermal conductivity of moist air ($J\ cm^{-1}\ s^{-1}\ K^{-1}$), T is temperature (K), and R^* is the universal gas constant (8.3145 $J\ mol^{-1}\ K^{-1}$).

[24] The solution to growth is an extension of the method developed by *Jacobson* [1997b, 2002b]. Integrating equations (4) and (5) for one size bin over a time step h gives

$$c_{L,Ni,t} = c_{L,Ni,t-h} + h k_{L,Ni,t-h} \left(C_{v,t} - S'_{L,Ni,t-h} C_{s,L,t-h} \right) \tag{14}$$

and

$$c_{I,Ni,t} = c_{I,Ni,t-h} + h k_{I,Ni,t-h} \left(C_{v,t} - S'_{I,Ni,t-h} C_{s,I,t-h} \right), \tag{15}$$

respectively, where the final gas mole concentration in both cases, $C_{v,t}$ is currently unknown. Final hydrometeor and gas concentrations are constrained by the gas-hydrometeor mass-balance equation,

$$C_{v,t} + \sum_{N=1}^{N_T} \sum_{i=1}^{N_B} \left(c_{L,Ni,t} + c_{I,Ni,t} \right) = C_{v,t-h} + \sum_{N=1}^{N_T} \sum_{i=1}^{N_B} \cdot \left(c_{L,Ni,t-h} + c_{I,Ni,t-h} \right) = C_{\mathrm{tot}}. \tag{16}$$

Substituting equations (14) and (15) into equation (16) and solving for $C_{v,t}$ gives a generalized solution for simultaneous condensation/evaporation and deposition/sublimation,

$$C_{v,t} = \frac{C_{v,t-h} + h \sum_{N=1}^{N_T} \sum_{i=1}^{N_B} \left(k_{L,Ni,t-h} S'_{L,Ni,t-h} C_{s,L,t-h} + k_{I,Ni,t-h} S'_{I,Ni,t-h} C_{s,I,t-h} \right)}{1 + h \sum_{N=1}^{N_T} \sum_{i=1}^{N_B} \left(k_{Li,t-h} + k_{Ii,t-h} \right)}. \tag{17}$$

Equation (17) is limited by $C_{v,t} = \mathrm{MIN}(C_{v,t}, C_{\mathrm{tot}})$, since the explicit condensation term in equation (17) can result in gas concentrations in excess of the maximum gas in the system. Equation (17) cannot fall below zero in any situation. $C_{v,t}$ is substituted back into equations (14) and (15) to give the final hydrometeor concentrations in each size bin. Since equations (14) and (15) can result in negative concentrations or concentrations above the maximum, two limits are placed sequentially, after equations (14) and (15) are solved. The first is $c_{L,N,i,t} = \mathrm{MAX}(c_{L,N,i,t}, 0)$; $c_{I,N,i,t} = \mathrm{MAX}(c_{I,N,i,t}, 0)$.

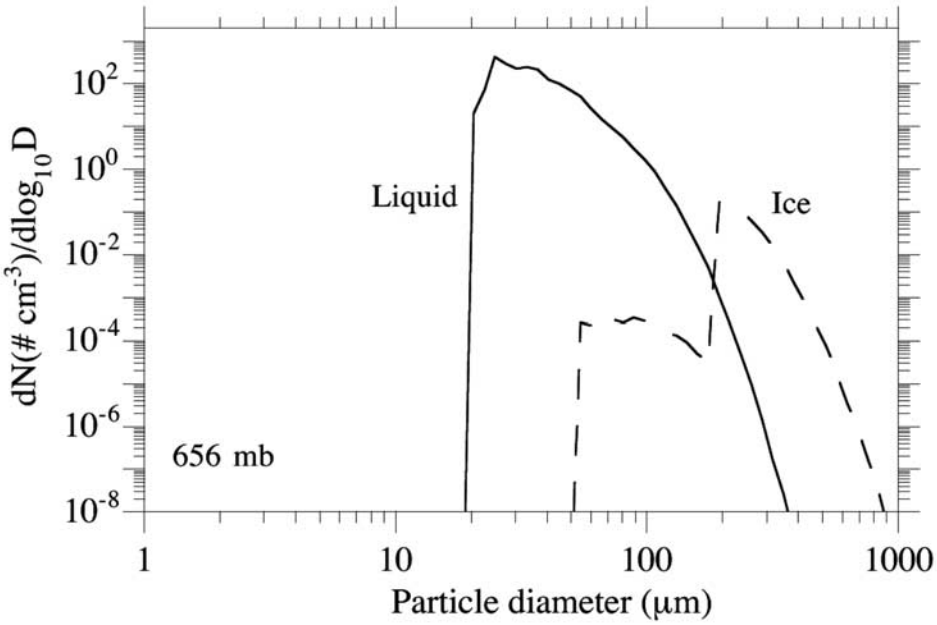

Figure 4. Condensed water on 16 CCN distributions and deposited on 16 IDN distributions simultaneously after a single 1-hour time step at 656 mb in the one-dimensional simulation. The figure shows the summation of water over all activated CCN and IDN distributions, respectively. Each CCN and IDN distribution was generated from an initial aerosol distribution, such as shown in Figure 3, but for a higher altitude.

The second, shown for liquid (the equation for ice uses $c_{I,N,i,t} - c_{I,N,i,t-h}$ instead of $c_{L,N,i,t} - c_{L,N,i,t-h}$ in the rightmost term) is

$$c_{L,Ni,t} = \frac{\left\{C_{v,t-h} - C_{v,t} + \sum_{N=1}^{N_T}\sum_{i=1}^{N_B}\left\{\mathrm{MAX}\left[c_{L,Ni,t-h} - c_{L,Ni,t}, 0\right] + \mathrm{MAX}\left[c_{I,Ni,t-h} - c_{I,Ni,t}, 0\right]\right\}\right\}}{\sum_{N=1}^{N_T}\sum_{i=1}^{N_B}\left\{\mathrm{MAX}\left[c_{L,Ni,t} - c_{L,Ni,t-h}, 0\right] + \mathrm{MAX}\left[c_{I,Ni,t} - c_{I,Ni,t-h}, 0\right]\right\}} \cdot\left(c_{L,Ni,t} - c_{L,Ni,t-h}\right), \quad (18)$$

where all $c_{L,N,i,t}$ and $c_{I,N,i,t}$ values on the right side of the equation are determined from equations (14) and (15), respectively, after the first limit has been applied. Equation (18) states that the final concentration is set to the net loss in vapor due to growth ($c_{v,t-h} - c_{v,t}$) plus the vapor gained by evaporation and/or sublimation, all scaled by the rate of condensation into the bin ($c_{L,N,i,t} - c_{L,N,i,t-h}$) divided by the sum of the rates of condensation and deposition into all bins. The solution in equations (14151617–18) is exactly mass conserving between the gas and hydrometeors under all conditions and is noniterative and positive-definite.

[25] Figure 4 shows the result of simultaneous condensation and deposition onto 32 distributions (16 CCN and 16 IDN distributions) at 656 mb after a single 1-h time step in the one-dimensional simulation. The distributions originated from these are shown in Figure 3, but for a higher altitude. Results were summed among activated liquid and ice hydrometeors among the distributions to produce the two curves in the figure. The shape of each distribution was affected by the shapes of the activated CCN and IDN distributions, as discussed subsequently.

[26] Figure 5a shows condensation onto 16 CCN distributions simultaneously in each of the five all-liquid altitude layers, assuming a critical radius and supersaturation from equation (10). Figure 5b shows results from the same simulation, except that all particles >0.2 μm diameter in all distributions were activated. In both cases, the mean hydrometeor diameter from condensation was smallest in the lowest layers because even after convection, aerosol concentrations increased with decreasing altitude (Figure 2). Increases in mean cloud drop diameter with increasing height have been observed [e.g., Figure 2.12b of *Pruppacher and Klett*, 1997]. In Figure 5a, condensation produced two peaks close to each other in diameter space in some layers. Such dual peaks, which have also been observed [e.g., Figures 2.25 and 2.12a of *Pruppacher and Klett*, 1997], arose because different distributions activated at different diameters, causing discontinuities in the summed size distribution of activated particles, causing slightly separate peaks. When the activation diameter was held constant over all distributions (Figure 5b), only one peak arose for each layer. Single peaks are also widely observed, suggesting that whether one or two peaks exist in the cloud size distribution following condensation may depend on the activation properties of the underlying aerosols, which depend on composition, surface tension, etc. Once dual peaks form, it is possible that the larger peak preferentially coagulates to larger sizes (peak separation), or that preferential sedimentation causes the larger peak to disappear from the layer faster. Preferential freezing of the larger peak could also lead to differentiation.

4.2. Partitioning From a Moving to Fixed Grid

[27] As a result of the previous step, each aerosol distribution N is split into activated CCN, activated IDN, and interstitial aerosol. Activated CCN, denoted here as distribution lq, contain liquid water (L) and all the aerosol

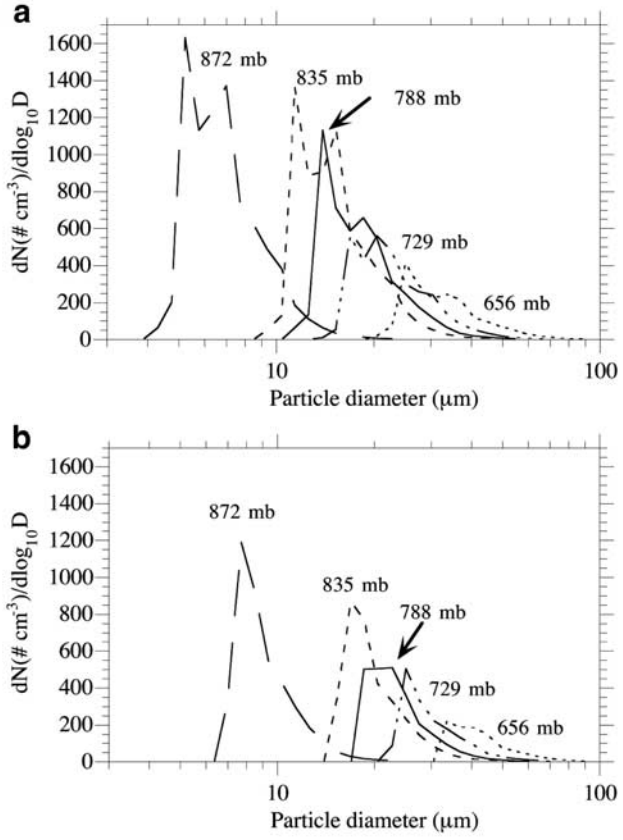

Figure 5. Condensed water on 16 CCN distributions simultaneously (h = 3600 s), in each of five layers in which the temperature was above 0°C in the one-dimension simulation when cloud activation was (a) determined from equation (10) and (b) assumed to occur for all particles >0.2 μm in diameter in all distributions. The figure shows the summation of water over all activated CCN in each layer.

constituents of the original CCN. Activated IDN (distribution ic), contain ice (I) and aerosol constituents. The total volume of a single grown liquid drop in a liquid distribution (lq) that forms on aerosol particles in bin i of distribution N is now $\upsilon_{\mathrm{lq},Ni} = v_{T,\mathrm{lq},Ni}/n_{\mathrm{lq},Ni}$, where

$$v_{T,\mathrm{lq},Ni} = v_{L,\mathrm{lq},Ni} + v_{s,\mathrm{lq},Ni} + \sum_{q=1}^{N_{\mathrm{NS}}} v_{q,\mathrm{lq},Ni} \tag{19}$$

is the total volume concentration (cm^3 cm^{-3}) of the hydrometeor. It consists of the volume concentration of liquid water ($v_{L,\mathrm{lq},Ni} = m_w c_{L,Ni}/\rho_L$), the volume concentration of an aerosol solution, and the volume concentrations of all nonsolution aerosol components (determined from mole concentrations). Similar equations are written for ice.

[28] The growth calculation assumed hydrometeors grew to their exact size without consideration of bin boundaries (moving bin method). For coagulation, in particular, it is often useful to use fixed (stationary) size bins. As such, hydrometeors and their components are rebinned here to fixed-bin hydrometeor size distributions. The volume concentration of total hydrometeor in original moving bin i is rebinned between two adjacent fixed bins, k and k + 1, in a new hydrometeor distribution (with N_C size bins) with $v_{T,\mathrm{lq},Nk} = f_{v,\mathrm{lq},Ni,k} v_{T,\mathrm{lq},Ni}$ and $v_{T,\mathrm{lq},Nk+1} = (1 - f_{v,\mathrm{lq},Ni,k}) v_{T,\mathrm{lq},Ni}$, where

$$f_{v,\mathrm{lq},Ni,k} = \left(\frac{\upsilon_{k+1} - \upsilon_{\mathrm{lq},Ni}}{\upsilon_{k+1} - \upsilon_k}\right)\frac{\upsilon_k}{\upsilon_{\mathrm{lq},Ni}} \tag{20}$$

is the volume fraction of particles from bin i partitioning into bin k. Volume concentrations of liquid water and aerosol solution and the mole concentration of all individual aerosol components are similarly partitioned. The number concentration of each moving bin k is partitioned with $n_{\mathrm{lq},Nk} = f_{n,\mathrm{lq},Ni,k} n_{\mathrm{lq},Ni}$ and $n_{\mathrm{lq},Nk+1} = (1 - f_{n,\mathrm{lq},Ni,k}) n_{\mathrm{lq},Ni}$, where

$$f_{n,\mathrm{lq},Ni,k} = \frac{\upsilon_{k+1} - \upsilon_{\mathrm{lq},Ni}}{\upsilon_{k+1} - \upsilon_k} \tag{21}$$

is the number fraction of particles from bin i partitioning into bin k. This method conserves number and volume exactly. At this point, it is possible to treat a separate liquid and ice size distribution for each aerosol distribution. Alternatively, all liquid and ice distributions can be summed separately over all aerosol distributions to produce one liquid and one ice distribution. This is done here to minimize computational time. With respect to total volume and number concentrations in the liquid hydrometeor distribution, the summations are

$$v_{T,\mathrm{lq},k} = \sum_{N=1}^{N_T} v_{T,\mathrm{lq},Nk} \quad n_{\mathrm{lq},k} = \sum_{N=1}^{N_T} n_{\mathrm{lq},Nk} = \frac{v_{T,\mathrm{lq},k}}{\upsilon_k}. \tag{22}$$

Similar summations are performed for liquid volume concentration, aerosol solution volume concentration, and aerosol solution and nonsolution component mole concentrations, and the same parameters for the ice distribution.

4.3. Hydrometeors Settling From Above and Melting of Hydrometeors From Above

[29] The next step is to add hydrometeors and their aerosol components that have settled from the layer above to the distributions generated from condensation/deposition in the current layer. The quantity of material settled to the current layer is given in section 4.8. Ice and graupel settled from the layer above are then melted if the ambient temperature is above the ice melting point, determined as [*Rasmussen and Pruppacher*, 1982]

$$T_{\mathrm{melt}} = T_0 + \mathrm{MAX}\left\{\frac{D_v L_e}{k_m R_v}\left[\frac{p_{v,s}(T_0)}{T_0} - \frac{p_v}{T_a}\right], 0\right\}. \tag{23}$$

Here T_0 = 273.15 K, $p_{v,s}(T_0)$ is the saturation vapor pressure (mb) at T_0, T_a is the ambient air temperature (K), p_v is the ambient partial pressure of water vapor (mb), D_v is the diffusion coefficient of water vapor in air (cm^2 s^{-1}), L_e is the latent heat of evaporation (J g^{-1}), κ_m is the thermal conductivity of moist air (J cm^{-1} s^{-1} K^{-1}), and R_v is the gas constant for water vapor (4614 cm^3 mb g^{-1} K^{-1}). This equation suggests that, when an ice particle begins to melt in subsaturated air, evaporative cooling of the meltwater delays melting of the overall particle. The lower the relative humidity (reflected in p_v), the greater the evaporative cooling, and the higher the melting temperature. When

melting occurs, the mass (g) of ice melted in a particle is [*Rasmussen et al.*, 1984]

$$\Delta m_{\mathrm{ic},Ni} = \mathrm{MIN}\left\{ -h\frac{4\pi r_{Ni}}{L_m}\left[k_m(T_a - T_0)F_{h,I,Ni} - \frac{D_v L_e}{R_v} \cdot\left(\frac{p_{v0,s}(T_0)}{T_0} - \frac{p_v}{T_a}\right)F_{v,I,Ni}\right], 0\right\}, \quad (24)$$

where L_m is the latent heat of melting (J g^{-1}) and h is the time step (s). It is assumed here that, instead of each ice/graupel particle of a given size containing the same fraction meltwater, a fraction of all ice/graupel particles of a given size by number, determined as $-\Delta m_{\mathrm{ic},Ni}/m_{\mathrm{ic},Ni}$ (where $m_{\mathrm{ic},Ni}$ is the mass of a single particle of that size), is converted to liquid. Temperatures are adjusted accordingly. Hydrometeor evaporation/sublimation during settling is discussed in section 4.10.

4.4. Hydrometeor-Hydrometeor Coagulation

[30] Next, coagulation is treated among hydrometeors that have grown in the current layer and settled from the layer above. Liquid drops and ice crystals are self-coagulated (liquid plus liquid or ice plus ice) to form larger liquid or ice particles and heterocoagulated (liquid plus ice) to form graupel, to simulate collision/coalescence. During hydrometeor self- and heterocoagulation, aerosol-particle components incorporated within hydrometeors are also coagulated. When liquid hydrometeors coagulate with ice or graupel to form graupel, temperatures are adjusted to account for CF.

[31] Several previous schemes for discretizing and solving the integro-differential equations for hydrometeor-hydrometeor coagulation (HHC) have been developed [e.g., *Tzivion et al.*, 1987; *Hounslow et al.*, 1988; *Lister et al.*, 1995; *Bott*, 2000, among others]. All such schemes conserve various properties, but they are explicit; thus their time step is limited by stability constraints. The scheme here is semi-implicit, positive definite, and unconditionally stable, and noniterative, with no limitation on time step. It is an extension of the scheme described by *Jacobson et al* [1994] and modified by *Jacobson* [2002b] for multiple aerosol size distributions interacting with each other. The solution method is exactly volume conserving and exactly volume concentration (number concentration multiplied by volume) conserving. Here the solution is adapted to any number of hydrometeor size distributions, size bins in each distribution, and component in each distribution. The final volume concentration of component x in particles of hydrometeor distribution Y in bin k at time t during coagulation is determined as

$$v_{x,Yk,t} = \frac{v_{x,Yk,t-h} + h(T_1 + T_2)}{1 + hT_3}, \quad (25)$$

where

$$T_1 = \sum_{M=1}^{N_H}\left[P_{Y,M}\sum_{j=1}^{k}\left(n_{Mj,t-h}\sum_{i=1}^{k-1}f_{Yi,Mj,Yk}\beta_{Yi,Mj,t-h}v_{x,Yi,t}\right)\right],$$

$$T_2 = \sum_{M=1}^{N_H}\sum_{I=1}^{N_H}\left[Q_{I,M,Y}\sum_{j=1}^{k}\left(n_{Mj,t-h}\sum_{i=1}^{k}f_{Ii,Mj,Yk}\beta_{Ii,Mj,t-h}v_{x,Ii,t}\right)\right],$$

and

$$T_3 = \sum_{j=1}^{N_C}\left[\sum_{M=1}^{N_H}\left[(1 - L_{Y,M})(1 - f_{Yk,Mj,Yk}) + L_{Y,M}\right]\beta_{Yk,Mj,t-h}n_{Mj,t-h}\right],$$

where N_H is the total number of hydrometeor distributions and N_C is the number of bins in each distribution. In this case, N_H = 3, where distributions Y and M = lq for the liquid distribution, ic for ice, and gr for graupel. The component x can be total hydrometeor volume concentration ($v_{T,\mathrm{lq}}$ $v_{T,\mathrm{ic}}$, or $v_{T,\mathrm{gr}}$), liquid water or ice concentration in the hydrometeor ($v_{L,\mathrm{lq}}$, $v_{I,\mathrm{ic}}$, or $v_{I,\mathrm{gr}}$), aerosol core solution concentration ($v_{s,\mathrm{lq}}$, $v_{s,\mathrm{ic}}$, or $v_{s,\mathrm{gr}}$), or any aerosol component volume concentration ($v_{q,\mathrm{lq}}$, $v_{q,\mathrm{ic}}$, or $v_{q,\mathrm{gr}}$). If it is total volume concentration, then total hydrometeor number concentration (n_{lq}, n_{ic}, or n_{gr}) equals total hydrometeor volume concentration in bin k divided by υ_k (e.g., $n_{\mathrm{lq},k,t} = v_{T,\mathrm{lq},k,t}/\upsilon_k$). Alternatively, a number concentration equation can be solved directly, but the result is identical.

[32] In the equation, $\beta_{Yi,Mj,t-h}$ is the coagulation rate coefficient (cubic centimeters per particle per second) between a particle in size bin i of distribution Y and a particle in bin j of distribution M, and $f_{Ii,Mj,Yk}$ is the fraction of the summed single-particle volume $V_{Ii,Mj} = \upsilon_{Ii} + \upsilon_{Mj}$ partitioned into bin k of distribution Y. Because the size bin structure used here for hydrometeor coagulation is a fixed (stationary) structure, volume fractions are calculated only once, during model initialization, with

$$f_{Ii,Mj,Yk} = \begin{cases} \left(\dfrac{\upsilon_{Yk+1} - V_{Ii,Mj}}{\upsilon_{Yk+1} - \upsilon_{Yk}}\right)\dfrac{\upsilon_{Nk}}{V_{Ii,Mj}} & \upsilon_{Yk} \le V_{Ii,Mj} < \upsilon_{Yk+1}\ k < N_C \\ 1 - f_{Ii,Mj,Yk-1} & \upsilon_{Yk-1} < V_{Ii,Mj} < \upsilon_{Yk}\ k > 1 \\ 1 & V_{Ii,Mj} \ge \upsilon_{Yk} \qquad k = N_C \\ 0 & \text{all other cases} \end{cases}. \quad (26)$$

[33] Finally, P, Q, and L are either 1 or 0, depending on the coagulation interactions accounted for. The parameter $P_{Y,M}$ = 1 if particles in distribution Y coagulating with particles in distribution M produce larger particles in distribution Y. If lq is the liquid distribution, ic is the ice distribution, and gr is the graupel distribution, then $P_{\mathrm{lq,lq}}$, $P_{\mathrm{ic,ic}}$, $P_{\mathrm{gr,gr}}$, $P_{\mathrm{gr,lq,}}$ and $P_{\mathrm{gr,ic}}$ = 1, but all other interactions are zero. The parameter $Q_{I,M,Y}$ = 1 if particles in distribution I coagulating with particles in distribution M produce particles in distribution Y, where $I \neq M$ and $I \neq Y$. For example, $Q_{\mathrm{lq,ic,gr}}$, $Q_{\mathrm{lq,gr,gr}}$, $Q_{\mathrm{ic,lq,gr}}$, and $Q_{\mathrm{ic,gr,gr}}$ = 1, but all other interactions are zero. The parameter $L_{Y,M}$ = 1 if particles in distribution Y coagulating with particles in distribution M do not produce particles in distribution Y. For example, $L_{\mathrm{lq,ic}}$, $L_{\mathrm{lq,gr}}$, $L_{\mathrm{ic,lq}}$, and $L_{\mathrm{ic,gr}}$ = 1, but all other interactions are zero.

[34] In equation (25), term T_1 accounts for production into distribution Y (any distribution) due to self-coagulation (e.g., $Y + Y$) and heterocoagulation of Y with a liquid or ice distribution M. Term T_2 accounts for production into distribution Y due to heterocoagulation of two independent distributions, I and M. The first part of term T_3 accounts for both self-coagulation loss ($Y + Y$) and heterocoagulation loss ($Y + M$) to larger sizes of the same distribution (N). The

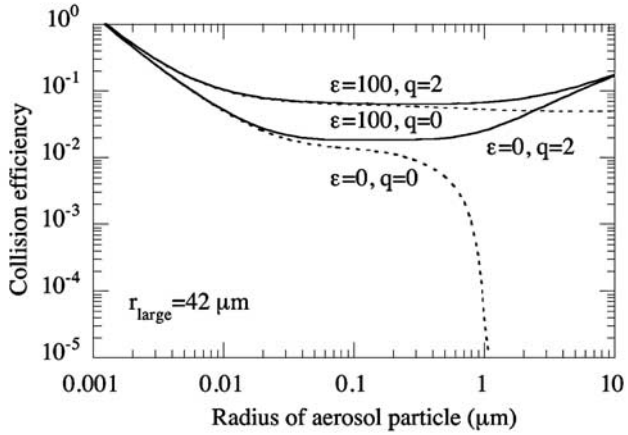

Figure 6. Collision efficiency of a 42-μm radius particle interacting with smaller particles for two dissipation rates (ε, $cm^2\ s^{-3}$) and two charge conditions (q, esu cm^{-2}). Other conditions were $T = 283.15$ K, $p = 900$ mb, and RH = 75%. The efficiency equaled the total coagulation kernel divided by $\pi(r_i + r_j)^2|V_{f,j} - V_{f,i}|$.

second part of T_3 accounts for heterocoagulation loss ($N + M$) to any distribution aside from N. Equation (25) is solved in a special order. Distributions that have no coagulation production from other distributions are solved first, followed by distributions with production terms from previously solved distributions. For example, distributions are solved in the order lq, ic, gr or ic, lq, gr. Within each distribution, equations are solved from bin $k = 1..N_C$. Each volume concentration distribution (x) can be solved in any order. To minimize computer time, all calculations involving a zero value of f, P, Q, or L are eliminated ahead of time.

[35] The total coagulation kernel in the model ($\beta_{\text{tot},Ii,Jj}$, cubic centimeters per particle per second) is the product of a coalescence efficiency ($E_{\text{coal},Ii,Jj}$) and a collision kernel ($K_{\text{tot},Ii,Jj}$, cubic centimeters per particle per second). Coalescence efficiencies are taken from the work of *Beard and Ochs* [1984] for small particle radius <50 μm and from the work of *Pruppacher and Klett* [1997] (equations (14–28)) for all other sizes. *Beard and Ochs* [1984] show that, due to the low kinetic energy of impact, the coalescence efficiency of particles <2 μm in radius with particles of any other size is unity. Coalescence efficiencies for larger-particle interactions are <1.

[36] The total collision kernel is a combination of kernels for Brownian motion, Brownian diffusion enhancement, turbulent inertial motion, turbulent shear, gravitational settling, thermophoresis, diffusiophoresis, and electric charge. The default kernels used here for the first five processes are described in equations 16.26–16.36 by *Jacobson* [1999].

[37] *Beard and Grover* [1974] derived a kernel from cloud-chamber measurements that accounts for Brownian motion, Brownian diffusion enhancement, and gravitational collection for 40 < large radius < 600 μm, small radius >1 μm, and small/large radius <0.1. Under these conditions, their kernel is used to override the corresponding default kernels.

[38] For nonoverlapping cases of 0.001 < small radius < 10 μm and 42 < large radius < 310 μm, the coagulation kernel is overridden further as follows. *Wang et al.* [1978] and *Martin et al.* [1980] derived overall collision kernels that accounted for gravitation, thermophoresis, diffusiophoresis, particle charge, Brownian motion, and Brownian diffusion enhancement, but not turbulent shear or turbulent inertial motion. Their kernel was in the form of the first expression below, which equals the second expression

$$K_{\text{tot},Ii,Jj} = \frac{4\pi B_{P,Ii} C_{Ii,Jj}}{\exp\left(B_{P,Ii} C_{Ii,Jj}/D_{p,Ii} r_j F_{p,Ii,Jj}\right) - 1} = \frac{4\pi B_{P,Ii} C_{Ii,Jj}}{\exp\left(4\pi B_{P,Ii} C_{Ii,Jj}/[K_B + K_{\text{DE}}]_{Ii,Jj}\right) - 1}. \quad (27)$$

In this equation, r_j is the big-particle radius (cm), $B_{P,Ii}$ is the mobility ($s\ g^{-1}$) of small particles of radius r_i (cm), $C_{Ii,Jj}$ is a complex parameter ($g\ cm^3\ s^{-2}$) that depends on charge, thermophoresis, and diffusiophoresis, $D_{p,Ii}$ is the diffusion coefficient ($cm^2\ s^{-1}$) of the small particle, $F_{p,Ii,Jj}$ is the ventilation coefficient for the small particle impacting the large particle, $K_{B,Ii,Jj}$ is the Brownian diffusion collision kernel (cubic centimeter per particle per second), $K_{\text{DE},Ii,Jj}$ is the Brownian diffusion enhancement collision kernel, and for the case of a small particle interacting with a large particle, $[K_B + K_{DE}]_{Ii,Jj} = 4\pi D_{p,i} r_i F_{p,i,j}$. If gravitational forces, charge, thermophoresis, and diffusiophoresis are ignored, equation (27) simplifies to $K_{\text{tot},Ii,Jj} = [K_B + K_{DE}]_{Ii,Jj}$. Here equation (27) is modified to account for kernels due to turbulent inertial motion (K_{TI}) and turbulent shear (K_{TS}). The result is

$$K_{\text{tot},Ii,Jj} = \frac{4\pi B_{P,Ii} C_{Ii,Jj}}{\exp\left(4\pi B_{P,Ii} C_{Ii,Jj}/[K_B + K_{\text{DE}} + K_{\text{TI}} + K_{\text{TS}}]_{Ii,Jj}\right) - 1}, \quad (28)$$

which simplifies to $K_{\text{tot},Ii,Jj} = [K_B + K_{\text{DE}} + K_{\text{TI}} + K_{\text{TS}}]_{Ii,Jj}$ in the absence of gravitation, charge, thermophoresis, and diffusiophoresis.

[39] Figure 6 shows modeled collision efficiencies of 42 μm radius particle interacting with smaller particles for two turbulent dissipation rates (ε, $cm^2\ s^{-3}$) and two charge conditions (q, esu cm^{-2}). The two curves for zero dissipation compare closely with curves 2 and 6 of Figure 4a of *Wang et al.* [1978]. The addition of turbulence affects collision efficiency the greatest when electric charge is zero. For nonzero or zero charge, turbulence increases collision efficiencies more for larger than smaller particles.

[40] Figure 7 shows individual collision kernels when ε = 100 $cm^2\ s^{-3}$, q = 2 esu cm^{-2}, and other conditions were

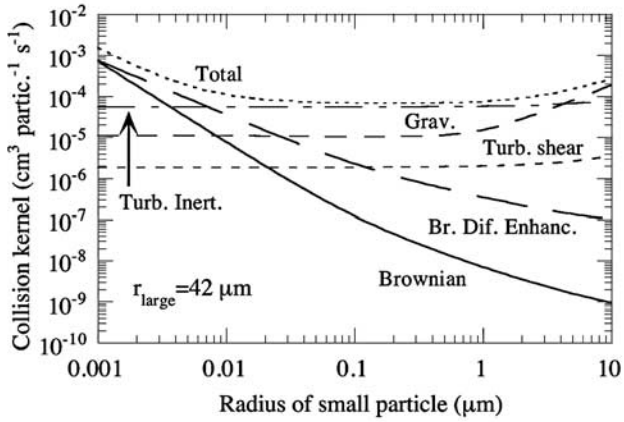

Figure 7. Individual and total collision kernels for the q = 2 and ε = 100 case in Figure 6.

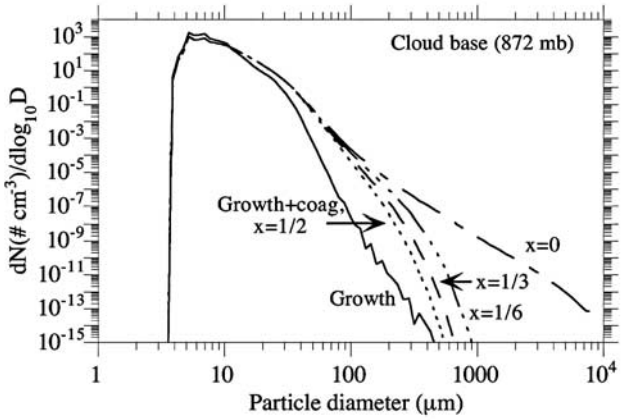

Figure 8. Coagulation, with a 1-hour time step, in the absence of settling from above, of a liquid distribution at cloud base that grew by condensation. Four coagulation cases are shown, each for a different x value in equation (29). The case $x = 0$ corresponds to concentrations for coagulation before sedimentation; $x = 1/2$ corresponds to concentrations after half a time step of sedimentation.

those shown in Figure 6. Brownian motion and diffusion enhancement dominated collision with a 42-μm particle when the second particle was of <0.01 μm radius. Turbulent inertia, which was strong in this case, dominated when the second particle was of 0.01–4 μm radius. Gravitational collection dominated for larger second particles.

[41] Figure 8 shows an example of coagulation of a liquid distribution following condensation, in the absence of settling from above. The time steps for growth and coagulation were 1 hour. The four coagulation results were obtained when coagulation kernels were modified with

$$K_{\text{tot},Ii,Jj,m} = \frac{K_{\text{tot},Ii,Jj,m}}{\left(1 + xhV_{f,Ii,m}/\Delta z_m\right)\left(1 + xhV_{f,Jj,m}/\Delta z_m\right)}, \quad (29)$$

where V_f is the hydrometeor fall speed (cm s^{-1}), Δz_m is the thickness of layer m, and x is a fraction, set to 0, 1/6, 1/3, and 1/2 in the four cases. Each term in the denominator represents a loss of initial concentration due to sedimentation from the layer during the coagulation time step. If $x = 0$, coagulation is solved as if no loss due to sedimentation occurs during the time step. This assumption is unrealistic, since it assumes that particles 5 mm in diameter are present in a layer for the same length of time as particles 10 μm in diameter. If $x = 1/2$, coagulation is solved as if the concentrations used for coagulation are those after a one half time step of sedimentation. Figure 8 shows that, when $x = 0$, coagulation produced particles almost 8 mm in diameter over 1 hour. When $x = 1/2$, the largest coagulated particles were <1 mm in diameter. For the bulk of this study, the result from $x = 1/3$, a compromise is used, although sensitivities with $x = 0$ are also discussed. An alternative to using equation (29) is to solve a half step of sedimentation prior to HHC (adjusting the concentration instead of the kernel). This is done for aerosol-hydrometeor coagulation, described shortly.

4.5. Liquid Drop Breakup

[42] Liquid-liquid self-coagulation can produce large raindrops that fall apart. One method of solving for drop breakup is to add breakup terms to the coagulation solution [e.g., *List and Gillespie*, 1976]. This method requires a fragment probability distribution for the interaction of each hydrometeor pair. A second method is to assume drops break up once they reach a critical size [e.g., *Danielsen et al.*, 1972]. This method requires a breakup distribution, which is similar to a fragment probability distribution, except that a breakup distribution is independent of the relative sizes of two colliding particles. Since coagulation is the primary method of producing large drops, the second method is similar to the first although the first allows some huge drops to persist longer. Since uncertainties of fragment probabilities are similar to those of breakup distributions, there is no advantage to the first method in this respect.

Table 1. Polynomial Coefficients for Drop Breakup in Equation (31)[a]

	$300 < d_k \leq 1290$ μm	$1290 < d_k \leq 5160$ μm
A_0	0.53098621799986	6.5418838298481
A_1	−0.0036655403240035	−0.0043878127949574
A_2	0.0000077765141976619	0.0000010066406670884
A_3	$-2.9695029431377 \times 10^{-9}$	$-7.771123366063 \times 10^{-11}$

[a]Coefficients were derived here by fitting data of *Danielsen et al.* [1972].

[43] Here raindrop breakup is treated by curve fitting the breakup distribution of *Danielsen et al.* [1972] so that it can be used for any size discretization. Drop breakup is assumed to occur when drops exceed 5 mm diameter. When this occurs, a mass fraction of the breakup drop is assigned to several bins. The mass fraction going to bin k is

$$\frac{dM}{M_T d\ \log_{10} D} d\ \log_{10}\ d_k \Bigg/ \sum_{j=1}^{N_C} \left(\frac{dM}{M_T d\ \log_{10} D} d\ \log_{10}\ d_k\right), \quad (30)$$

where d_k is the diameter (μm) and

$$\frac{dM}{M_T d\ \log_{10} D} = A_0 + d_k(A_1 + d_k(A_2 + d_k A_3)) \quad (31)$$

is a polynomial fit, derived here, to the breakup distribution of *Danielsen et al.* [1972] (dM is incremental mass, M_T is total mass, and D is diameter). Table 1 gives coefficients for equation (31). Figure 9 shows the breakup distribution from equation (31).

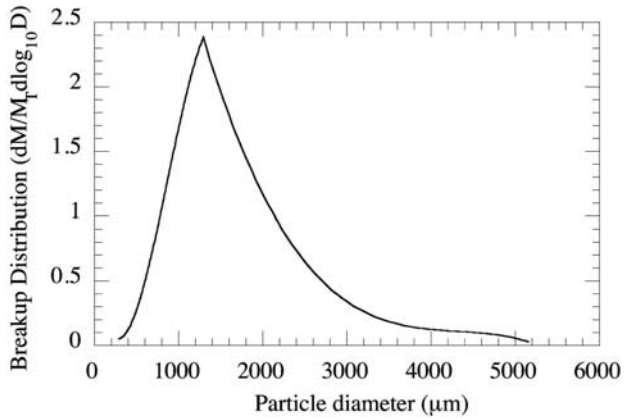

Figure 9. Raindrop breakup size distribution generated from equation (31), which was derived here as a fit to the breakup distribution of *Danielsen et al.* [1972].

4.6. Contact Freezing of Liquid Drops by Aerosol Particles

[44] Contact freezing (CF) is a mechanism by which aerosol ice contact nuclei (ICN) impact liquid drops at subfreezing temperatures, causing them to freeze to graupel. This process is treated here by coagulating size-resolved aerosols from all distributions with all sizes of liquid hydrometeors. The calculation assumes that if aerosol particles in an aerosol size bin contain active ICN and collide with drops in a liquid hydrometeor bin, a fraction of the population of contacted liquid drops and their components in the bin is transferred to the same bin in the graupel distribution. In-cloud temperatures are updated to account for latent heat release during CF.

[45] The loss of liquid hydrometeor total volume concentration or component volume concentration and the corresponding gain of graupel due to CF are

$$v_{x,\mathrm{lq},k,t} = \frac{v_{x,\mathrm{lq},k,t-h}}{1 + hT_3} \text{ where } T_3 = F_T \sum_{j=1}^{N_C} \left[\sum_{N=1}^{N_T} \beta_{Yk,Nj,t-h} F_{\mathrm{ICN},Nj} n_{Nj,t-h} \right] \tag{32}$$

and

$$v_{x,\mathrm{gr},k,t} = v_{x,\mathrm{gr},k,t-h} + v_{x,\mathrm{lq},k,t} hT_3, \tag{33}$$

respectively, where F_T is the temperature dependence of contact nucleation, $F_{\mathrm{ICN},Nj}$ is the fraction of the number concentration of particles in the size bin that are contact nuclei, and the final number concentrations in each bin of each distribution are $n_{\mathrm{lq},k,t} = v_{T,\mathrm{lq},k,t}/\upsilon_k$ and $n_{\mathrm{gr},k,t} = v_{T,\mathrm{gr},k,t}/\upsilon_k$. The temperature parameter is

$$F_T = \begin{cases} 0 & T > -3^\circ\mathrm{C} \\ -(T+3)/15 & -18 < T < -3^\circ\mathrm{C} \\ 1 & T < -18^\circ\mathrm{C} \end{cases}, \tag{34}$$

where T is in °C. This equation was obtained by noting that Figure 2 of *Pitter and Pruppacher* [1973] shows that kaolinite and montmorillonite contact freeze 100% of drops at −18°C and 0% of drops at −3°C. The product, $F_T F_{\mathrm{ICN},Nj} n_{Nj,t-h}$ is the number of contact nuclei in a given bin of a given aerosol distribution at a given temperature. Parameterizations of the total number of ICN at a given temperature are available [e.g., *Meyers et al.*, 1992] but are not used here for the same reason for which parameterizations of IDN are not used, as discussed earlier. Instead, $F_{\mathrm{ICN},Nj}$ is set to $F_{\mathrm{IDN},Nj}$, although this assumption is conservative because a higher fraction of aerosol components generally serve as ICN than IDN. A sensitivity was run (section 5.5) to test this assumption. CF is not allowed to affect aerosol distributions because aerosol coagulation with all hydrometeors is treated separately in section 4.9.

4.7. Homogeneous + Heterogeneous Freezing of Liquid Drops

[46] The model also treats homogeneous plus heterogeneous freezing (HHF). Heterogeneous freezing occurs when a drop contains an ice immersion nucleus (IIN). Immersion nuclei are not treated explicitly here because of the uncertainty in nucleation rate parameters for IIN. Instead, HHF is treated by fitting an equation to laboratory results of liquid drop freezing. This treatment is also uncertain, because it assumes that the composition of drops in the air is similar to that in laboratory experiments, which have often been performed with tap water. Thus it is uncertain whether the experiments simulated heterogeneous or homogeneous freezing or both.

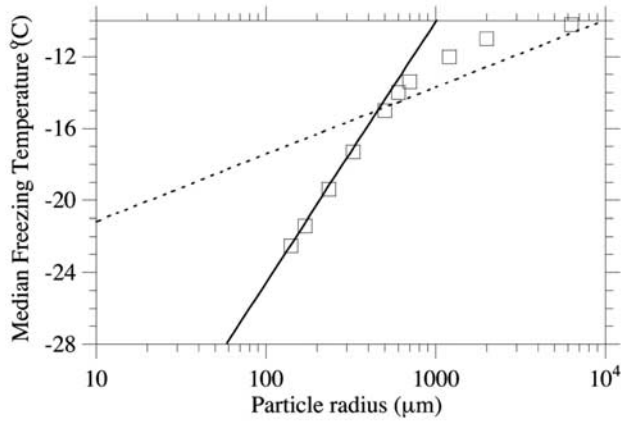

Figure 10. Comparison of fitted equations for median freezing temperature with data of *Pitter and Pruppacher* [1973, Figure 1], from which the fits were derived.

[47] Several studies have suggested that the HHF temperature is related logarithmically to drop volume [e.g., *Bigg*, 1953; *Vali*, 1971; *Pitter and Pruppacher*, 1973]. For heterogeneous freezing, this assumption is physical since ICN can be randomly distributed within a drop. Under this theory, the fractional number of drops that freeze is

$$F_{\mathrm{Fr},k,t} = \upsilon_{L,\mathrm{lq},k} \exp[-B(T - T_r)], \tag{35}$$

where T is the temperature of a population of drops (°C), T_r is a reference temperature (°C), and B is a fitting coefficient (°C^{-1}). Since the equation is empirical, units do not equate. From this equation, the median freezing temperature, which is the temperature at which 50% of drops freeze ($F_{\mathrm{Fr}} = 0.5$), is

$$T_m = T_r - \frac{1}{B} \ln\left(\frac{0.5}{\upsilon_{L,\mathrm{lq},k}}\right). \tag{36}$$

Several values of B and T_r have been derived from laboratory data [e.g., *Danielsen et al.*, 1972; *Orville and Kopp*, 1977]. *Pitter and Pruppacher* [1973] showed experimentally that the freezing rate followed logarithmically with drop volume only for temperatures below −15°C. Here data from the work of *Pitter and Pruppacher* [1973, Figure 1, curve 1] are used to derive values of B and T_r (which they did not present) for below −15°C and separately for −15° to −10°C. For the former regime, B and T_r are found here to be 0.475°C^{-1} and 0°C, respectively. For the latter regime, they are 1.85°C^{-1} and −11.14°C, respectively. For the latter regime, the fit treats the volume dependence of their data correctly only at the extremes, but still represents an improvement over the use of one equation. Above −10°C, no drops are permitted to freeze. Figure 10 compares the fits to the original data.

[48] Equation (36) is an equilibrium equation. A time-dependent freezing-rate equation is

$$\frac{dn_{\mathrm{gr},k,t}}{dt} = n_{\mathrm{lq},k,t-h}\upsilon_{L,\mathrm{lq},k}A\ \exp[-B(T-T_r)], \tag{37}$$

where $A = 10^{-4}$ cm^{-3} s^{-1} [e.g., *Reisin et al.*, 1996; *Orville and Kopp*, 1977]. Integrating this equation gives the changes in liquid and graupel number concentration over time step h as $n_{\mathrm{lq},k,t} = n_{\mathrm{lq},k,t-h}(1 - F_{\mathrm{FR},k,t})$ and $n_{\mathrm{gr},k,t} = n_{\mathrm{gr},k,t-h}$ $n_{\mathrm{gr},k,t-h} + n_{\mathrm{lq},k,t\text{-}h}\ F_{\mathrm{Fr},k,t}$, respectively, where

$$F_{\mathrm{Fr},k,t} = 1 - \exp\{-hA\upsilon_{L,\mathrm{lq},k}\ \exp[-B(T-T_r)]\}. \tag{38}$$

Component volume concentrations are similarly partitioned between liquid and ice. The median freezing temperature from this equation is

$$T_m = T_r - \frac{1}{B}\ln\left(\frac{\ln(0.5)}{hA\upsilon_{L,\mathrm{lq},k}}\right). \tag{39}$$

Equating equations (39) and (36) suggests that the time for equilibration when $A = 10^{-4}$ cm^{-3} s^{-1} is $h_{\mathrm{eq}} = \ln(0.5)/(0.5\ A) = 13{,}862$ s, which is much greater than the time step for model processes. In-cloud temperatures are updated to account for latent heat release during HHF.

4.8. Settling of Hydrometeors and their Aerosol Components

[49] Settling from a layer is calculated in two half time steps during the cloud time interval. Two half steps are taken because for processes such as aerosol-hydrometeor coagulation and cloud chemistry, it is desirable to have parameter values at the middle, rather than beginning or end, of the interval. Thus after the first settling calculation, some processes are solved. The settling procedure is a standard implicit, noniterative, unconditionally stable, and exactly mass- and number-conserving scheme. As applied here, it permits a solution one layer at a time that gives the same solution as if all layers were solved simultaneously over the same time step. The advantage of solving one layer at a time is that many operator-split processes can be treated in each layer that affect layers below.

[50] The loss of total or component volume concentration in a size bin during two half steps of settling is

$$v_{x,Y,k,t-\frac{1}{2}h,m} = v_{x,Y,k,t-h,m}\Bigg/\left(1 + \frac{h}{2}\frac{V_{f,Y,k,m}}{\Delta z_m}\right), \tag{40}$$

$$v_{x,Y,k,t,m} = v_{x,Y,k,t-\frac{1}{2}h,m}\Bigg/\left(1 + \frac{h}{2}\frac{V_{f,Y,k,m}}{\Delta z_m}\right), \tag{41}$$

where several processes are solved between the two half time steps. At the end of the two half steps, the corresponding gain to the layer below is

$$v_{x,Y,k,t-h,m+1} = v_{x,Y,k,t-h,m+1} + \frac{h}{2}\frac{V_{f,Y,k,m}}{\Delta z_m}\frac{\Delta z_m}{\Delta z_{m+1}} \cdot\left(v_{x,Y,k,t-\frac{1}{2}h,m} + v_{x,Y,k,t,m}\right), \tag{42}$$

where the gain is added to time $t - h$ to ensure the solution for one layer at a time that exactly matches for all layers simultaneously. Here V_f is the fall speed (cm s^{-1}). The fall speeds for liquid drops are calculated from the work of *Beard* [1976], who covered the size range 0.5 μm–7 mm. Fall speeds for ice and graupel are similar, except that Reynolds numbers and fall speed are adjusted for shape assuming ice and graupel are hexagonal plates and oblate spheroids, respectively. Shape factors used are from the studies of *Fuchs* [1964] and *Turco et al.* [1982].

[51] The material added to layer $m + 1$ is precipitation passing to that layer. If layer m is the bottom layer, $v_{x,Y,k,t-h,\ m+1}\Delta z_{m+1}$ (where Δz_{m+1} at the surface can have any value since it cancels out) represents precipitation per unit area of hydrometeors and their aerosol components to the surface. The liquid water content (cm^3 cm^{-3}) of precipitation in any layer, used shortly for gas rainout, is $p_{L,\mathrm{lq},k,t,m+1} = v_{L,\mathrm{lq},k,t-h,\ m+1}$ and is obtained at the end of the two half steps of settling. Precipitation falling into a layer is added to new hydrometeors produced in this layer, as described in section 4.3.

4.9. Aerosol-Hydrometeor Coagulation: Aerosol Washout

[52] Following the first half step of settling, aerosol particles from all aerosol distributions are coagulated with each hydrometeor distribution, reducing the number of aerosol particles and increasing the volume of hydrometeor particles and aerosol components trapped within hydrometeors by the corresponding loss in interstitial aerosol. Since aerosol particles that coagulate with hydrometeor particles can sediment to lower layers, aerosol-hydrometeor coagulation is part of the washout process.

[53] The aerosol-hydrometeor coagulation loss for aerosols and their components is

$$v_{x,Nk,t} = \frac{v_{x,Nk,t-h}}{1 + hT_3} \quad T_3 = \sum_{j=1}^{N_C}\left[\sum_{M=1}^{N_H}\beta_{Nk,Mj,t-h}n_{Mj,t-h}\right], \tag{43}$$

where the integration is performed over the entire time step (h), but the initial values for hydrometeors are those obtained following the first half step of settling (t and $t - h$ are still used since the time interval for the calculation is h). The corresponding volume-conserving production of hydrometeors and aerosol components within hydrometeors is

$$v_{x,Yk,t} = \frac{v_{x,Yk,t-h} + h(T_1 + T_2)}{1 + hT_3}, \tag{44}$$

where

$$T_1 = \sum_{N=1}^{N_T}\left[\sum_{j=1}^{k}\left(n_{Nj,t-h}\sum_{i=1}^{k-1}f_{Yi,Nj,Yk}\beta_{Yi,Nj,t-h}v_{x,Yi,t}\right)\right],$$

$$T_2 = \sum_{N=1}^{N_T}\left[\sum_{j=1}^{k}\left(n_{Yj,t-h}\sum_{i=1}^{k}f_{Ni,Yj,Yk}\beta_{Ni,Yj,t-h}v_{x,Ni,t}\right)\right],$$

and

$$T_3 = \sum_{j=1}^{N_B}\left[\sum_{N=1}^{N_T}\left(1 - f_{Yk,Nj,Yk}\right)\beta_{Yk,Nj,t-h}n_{Nj,t-h}\right].$$

In addition, $n_{Nk,t} = v_{T,Nk,t}/\upsilon_k$ and $n_{Yk,t} = v_{T,Yk,t}/\upsilon_k$. The aerosol-hydrometeor coagulation kernels are calculated in the same manner as are those for HHC, accounting for thermophoresis, diffusiophoresis, charge, etc.

4.10. Below-Cloud Hydrometeor Evaporation/ Sublimation and Evaporative Freezing

[54] When hydrometeors settle to subsaturated layers below a cloud, they begin to evaporate/sublimate. The evaporation/sublimation rate of small hydrometeors is sufficiently fast that the entire hydrometeor may diminish to the aerosol core. Large hydrometeors, though, often survive to reach the surface. Evaporation/sublimation of a hydrometeor cools its surface. The treatment of evaporation/sublimation described here accounts for vapor exchange and change in surface temperature.

[55] The procedure for drop evaporation/crystal sublimation during settling is performed by first calculating the equilibrium drop or crystal surface temperature iteratively then solving for evaporation/sublimation using the resulting vapor gradient between the hydrometeor surface and ambient air. This procedure is based on the method of *Beard and Pruppacher* [1971] and *Pruppacher and Rasmussen* [1979] with modification. The process is calculated before the second half step of settling.

[56] In the case of a liquid drop, the iteration involves solving the following equations:

$$p_{s,n} = p_{v,s}(T_{s,n}),$$

$$p_{f,n} = 0.5(p_{s,n} + p_{v,n}),$$

$$T_{s,n+1} = T_{s,n} - \frac{D_v L_e}{\kappa_m(1 - p_{f,n}/p_a)} \frac{\Delta p_{v,n}}{R_v T_{f,n}}, \qquad (45)$$

$$p_{v,n+1} = p_{v,n} + \Delta p_{v,n},$$

$$\Delta p_{v,n} = 0.3[p_{s,n} - p_{v,n}],$$

$$T_{f,n} = 0.5(T_{s,n} + T_a),$$

where $T_{s,n}$ is the drop surface temperature (K) at iteration n, initialized at the ambient temperature T_a (K), which stays constant, $p_{s,n}$ is the saturation vapor pressure (mb) over the drop surface, evaluated at the drop surface temperature, $\Delta p_{v,n}$ is an estimated change in water vapor partial pressure at iteration n, $p_{f,n}$ and $T_{f,n}$ are average values of water vapor partial pressure and of temperature between the drop surface and ambient air, D_v is the diffusion coefficient of water vapor in air ($cm^2\ s^{-1}$), L_e is the latent heat of evaporation ($J\ g^{-1}$), κ_m is the thermal conductivity of moist air ($J\ cm^{-1}\ s^{-1}\ K^{-1}$), R_v is the gas constant for water vapor ($4614\ cm^3\ mb\ g^{-1}\ K^{-1}$), and p_a is the ambient air pressure (mb). The above set of equations is iterated a minimum of three times. The factor of 0.3 is included in $\Delta p_{v,n}$ to ensure convergence without overshooting. Otherwise, the equations differ from the study of *Beard and Pruppacher* [1971] only in that the present equations ignore ventilation coefficients for energy and vapor and radiative heating to eliminate the size-dependence of the iterative calculation, which would add to computer time without affecting the results significantly. For example, when size-dependent parameters are included, the difference in final drop surface temperature between a 0.001 and 1000 μm drop is only 2.5% (0.05 K/2 K) of the mean drop surface temperature depression when the relative humidity (RH) is 80% and the ambient temperature is 283.15 K. Even at an RH of 1%, the difference is only 4% (0.4 K/10 K). Temperature equations for sublimation are analogous to those for evaporation.

[57] Figure 11 shows the variation in equilibrium drop surface temperature and other parameters for initial RHs of 1–100% under (1) lower-tropospheric conditions, (2) midtropospheric conditions, and (3) upper-tropospheric conditions. The figure shows that, under lower-tropospheric conditions, drop surface temperatures can decrease by as much as 10 K when the ambient RH is 1%. At RH = 80%, which is more typical below a cloud, the temperature depression is close to 2 K. Under midtropospheric conditions, supercooled drop temperatures can decrease by as much as 2.2 K when they fall into regions of RH = 1% (Figure 11b) or 1 K if they fall into regions of 50% RH. Under upper-tropospheric conditions, the maximum temperature depression is about 0.5 K.

[58] After a drop's surface temperature is found, its evaporation rate is determined by

$$v_{L,\mathrm{lq},k,t,m} = \mathrm{MAX}\left[v_{L,\mathrm{lq},k,t-h} - \frac{n_{\mathrm{lq,k}} 4\pi dr_k D_v}{(1 - p_{f,nf}/p_a)} \frac{(p_{v,s,0} - p_{v,nf})}{\rho_L R_v T_{f,nf}} \cdot \frac{\Delta z}{V_{f,\mathrm{lq},k}}, 0 \right]_m, \qquad (46)$$

where the subscripts 0 and *nf* indicate initial and final values, respectively, from equation (45), and the time step over which evaporation occurs is determined as the layer thickness divided by the fall speed; thus it is the time the hydrometeor can last in the layer before falling to the next layer. This time step is physical since if the model time interval were used in the calculation, big drops with short lifetimes would evaporate in the model for a longer period than they actually last in the layer. Drops with long lifetimes will be evaporated anyway once the time interval is over. Water vapor and temperature in the model are adjusted following evaporation. Ice sublimation is calculated in a similar manner. Evaporation/sublimation is a moving bin calculation in the model. Following it, drops are rebinned to fixed bins with the volume- and number-conserving equations discussed in section 4.2. After rebinning, the second step of settling is performed.

[59] Figure 12 shows an example effect of evaporation on an idealized size distribution of precipitation drops reaching the surface after falling about 1 km from cloud base through air in which the RH was 99 and 75%. Evaporation eliminated small drops in both cases. Evaporation shrank drops more effectively at the lower RH, as expected. Subcloud evaporation added water vapor to the air below the cloud, as previously found experimentally and numerically, [e.g.,

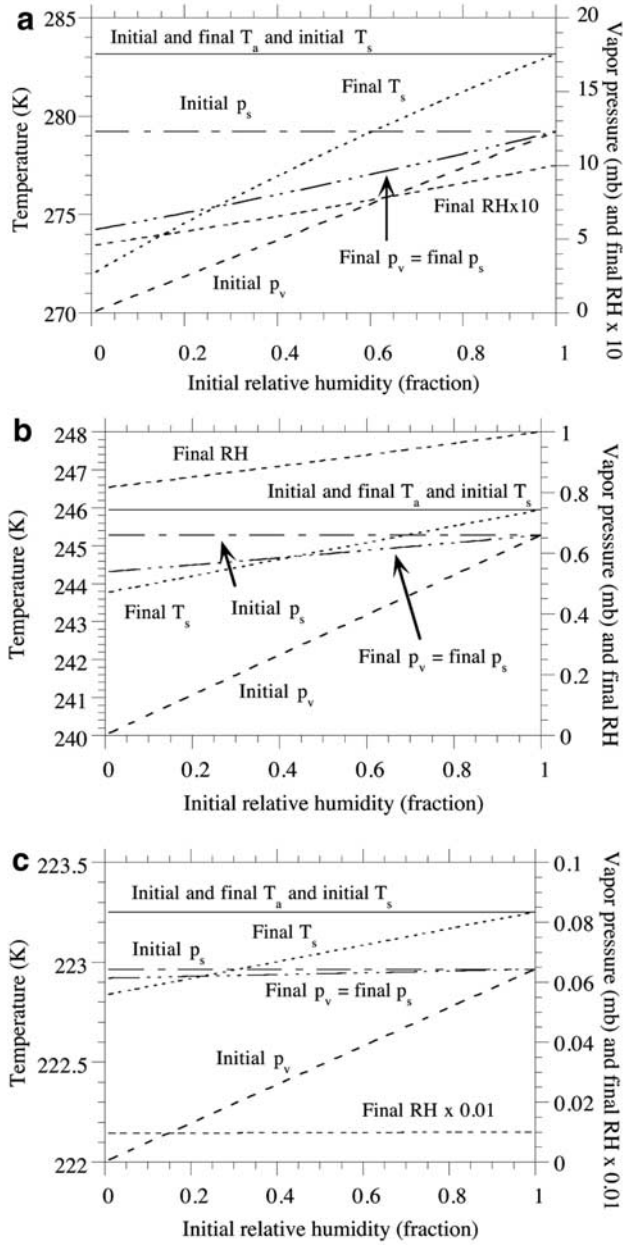

Figure 11. Variation in equilibrium liquid drop surface temperature (T_s, K), saturation vapor pressure over the drop surface (p_s, mb), partial pressure of water away from the drop surface (p_v, mb), and RH near the drop surface for initial ambient RHs of 1–100% when (a) the ambient temperature (T_a) = 283.15 K and air pressure (p_a) = 900 mb (lower tropospheric conditions) (b) T_a = 245.94 K and p_a = 440.7 mb (middle tropospheric conditions), and (c) T_a = 223.25 K and p_a = 265 mb (upper tropospheric conditions). The figure was obtained from equation (45).

Beard and Pruppacher, 1971; *Orville and Kopp*, 1977; *Pruppacher and Rasmussen*, 1979], potentially fueling additional cloud formation.

[60] A combination of Figures 11 and 10 suggests that evaporative cooling of liquid drops at their surface as they fall into regions of low RH under the right temperature and pressure conditions may be a mechanism of drop freezing. This proposed mechanism is referred to here as "evaporative freezing." Whenever a liquid drop falls through subsaturated air, it cools. If a large drop cools to below −10°C, the probability of heterogeneous freezing exceeds zero (Figure 10). As the drop cools more, the probability of freezing increases further. The onset of freezing and the median freezing temperature of small drops are lower than are those of large drops, but even for small drops, evaporative cooling may enhance the probability of freezing under the right conditions.

[61] When a drop freezes in air substaturated with respect to liquid, it begins to sublimate if the air is also subsaturated with respect to ice. Small crystals may sublimate altogether, but large drops may reach the surface as graupel. Even small drops that freeze then sublimate and may have an impact on radiative, aerosol, or cloud properties in the atmosphere while they are present, but this issue is not explored here.

[62] Figure 13 demonstrates modeled enhanced freezing due to evaporative cooling. The figure shows a liquid distribution at 100% RH. At RH = 81%, the subfreezing temperature (236.988 K) cooled by 0.35 K, increasing the number of frozen liquid drops by about 5% above the number frozen at 236.988 K (not shown in the figure).

[63] The theory, discussed here, that evaporative cooling at a drop's surface as the drop falls through subsaturated air may enhance its rate of freezing is analogous to the theory, shown experimentally by *Rasmussen and Pruppacher* [1982], that evaporative cooling delays the onset of melting.

[64] The evaporative freezing theory also implies that homogeneous/heterogeneous drop freezing in subsaturated air may occur first on a drop surface rather than in the bulk of the drop. Other authors have suggested that homogeneous/heterogeneous freezing is more likely to occur at a drop surface than in the bulk of a drop, but for different reasons. *Tabazadeh et al.* [2003], for example, found that ice nucleation is thermodynamically favored on the surface in comparison with the bulk of a liquid drop, even when no temperature gradient exists. *Stuart* [2002] found that, if a frozen nucleus forms in the middle of a drop, thin dendrites shoot out to the surface and warm the drop within less than 0.1 s. Heat loss by the partially frozen drop occurs only by

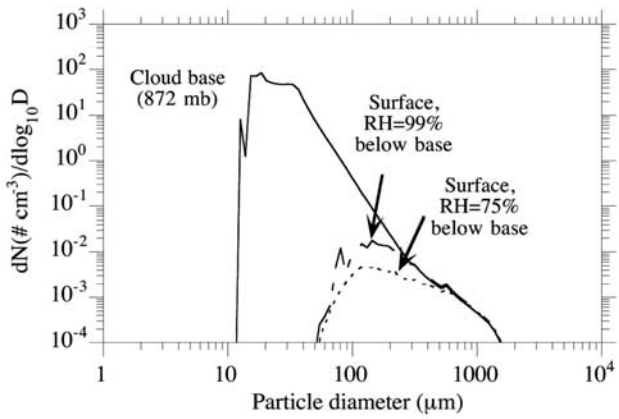

Figure 12. Effect of evaporation on the size distribution of precipitation drops reaching the surface after falling from a cloud base at about 1.5 km through subsaturated air in which the RH was 99 and 75%, respectively.

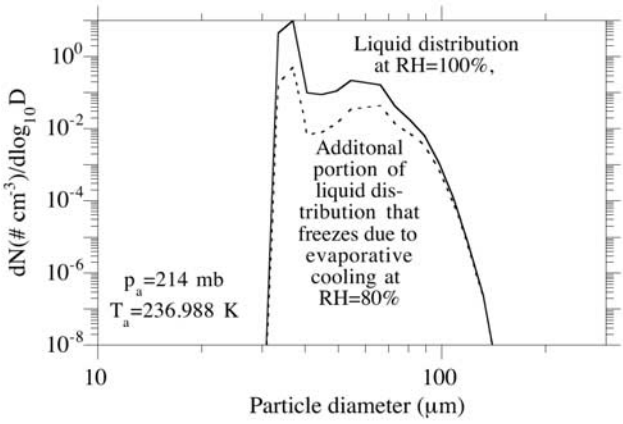

Figure 13. Additional homogeneous/heterogeneous freezing due to evaporative cooling. The figure shows a liquid size distribution at an ambient pressure of 214 mb, ambient temperature of 236.988 K, and RH of 100%. When the RH decreases to 80%, the drop surface temperature decreases to 236.617 K, causing 5% more liquid drops to freeze by homogeneous/heterogeneous nucleation than would otherwise have frozen at 236.988 K.

conduction and evaporation at the surface, causing the surface temperature to be cooler than the rest of the drop but warmer than the drop was originally. Due to the cooler surface relative to interior, remaining freezing proceeds from the surface, inward. Thus although freezing initiates in the center, the rate of freezing quickly increases at the surface relative to the interior. The main difference between the mechanism of *Stuart* [2002] and pure evaporative freezing is that, with the former, surface freezing is triggered by heterogeneous or homogeneous freezing within the drop itself; with the latter, surface freezing is triggered by surface cooling as a drop falls through subsaturated air. Evaporative freezing can occur on its own or with one of these other mechanisms to enhance the rate of surface freezing.

4.11. Evaporation of Leftover Hydrometeors to Aerosol Cores, Large-Scale Precipitation

[65] Since the cumulus and stratus parameterizations for the next time interval of cloud calculations require water to be vapor, it is necessary to evaporate/sublimate remaining hydrometeors in each layer. When drops/crystals are evaporated/sublimated in a layer, their cores, which consist of solution and nonsolution components, remain. These components are rebinned to the most internally mixed aerosol distribution ($N = N_T$) with the technique from section 4.2. Following evaporation, supersaturated water is condensed or deposited in bulk, then dropped to the layer below, where it is converted back to vapor. This condensation/deposition procedure is iterative and adjusts temperature [*Arakawa and Lamb*, 1977]. If excess water remains at the bottom, it is treated as large-scale precipitation.

4.12. Gas-Hydrometeor Dissolution: Gas Washout

[66] Gas washout is solved progressively from the topmost cloud layer to the surface by considering that gas dissolved in bulk rainwater from a layer above is carried to a current layer, where it affects the solubility of the gas in the current layer. The numerical solution is derived by considering the gas-hydrometeor equilibrium equation,

$$\frac{c_{q,\mathrm{lq},t,m}}{C_{q,t,m}} = H'_q R^* T \sum_{k=1}^{N_C} p_{L,\mathrm{lq},k,t,m} \tag{47}$$

and the gas-hydrometeor mass-balance equation

$$C_{q,t,m} + c_{q,\mathrm{lq},t,m} = C_{q,t-h,m} + c_{q,\mathrm{lq},t,m-1} \frac{\Delta z_{m-1}}{\Delta z_m}, \tag{48}$$

where $C_{q,t,m}$ is the mole concentration of gas q, $c_{q,\mathrm{lq},t,m}$ is the total (summed over all bins) mole concentration of the dissolved gas in the liquid distribution, $p_{L,\mathrm{lq},k,t,m}$ is liquid precipitation passing through layer m in bin k ($\mathrm{cm}^3\ \mathrm{cm}^{-3}$), R^* is the gas constant (0.08206 l atm mol^{-1} K^{-1}), H'_q is an effective Henry's constant for species q (mol l^{-1} atm^{-1}), and T is temperature (K). Equation (48) states that the final gas plus aqueous species concentration equals the initial gas concentration in the layer plus the aqueous concentration in precipitation from the layer above. For the top cloud layer, $c_{q,\mathrm{lq},t,m-1} = 0$. Combining Equations (47) and (48) gives the final gas concentration in layer m,

$$C_{q,t,m} = \frac{\left(C_{q,t-h,m} + c_{q,\mathrm{lq},t,m-1}\right) \dfrac{\Delta z_{m-1}}{\Delta z_m}}{1 + H'_q R^* T \displaystyle\sum_{k=1}^{N_C} p_{L,\mathrm{lq},k,t,m}}. \tag{49}$$

The aqueous-phase mole concentration, used for the next layer, is

$$c_{q,\mathrm{lq},t,m} = C_{q,t-h,m} + c_{q,\mathrm{lq},t,m-1} \frac{\Delta z_{m-1}}{\Delta z_m} - C_{q,t,m}. \tag{50}$$

This solution is exactly mass conserving, noniterative, unconditionally stable, and positive definite. It states that if rainwater passing through a cell is already saturated with gas, no additional gas can enter the rainwater, but some may be added to the current layer. This mechanism not only removes gases but also transfers gases from a supersaturated layer to a subsaturated layer. The treatment in this section is not applied to SO_2(g) because its concentration is affected by both dissolution and aqueous chemistry. These processes are treated in section 4.13. Aqueous reactions affect other species as well. Such reactions are readily treated, but due to computer limitations, they were not applied in this study.

4.13. Aqueous Chemistry

[67] SO_2(g) dissolution and oxidation in aerosol-particles, clouds, and rainwater is treated by solving the irreversible reactions, $SO_2(g) + H_2O_2 \rightarrow$ S(VI)(aq) and $SO_2(g) + O_3(g) \rightarrow$ S(VI)(aq) together with gas photochemistry (using an iterative chemical solver) to simulate dissolution and formation of S(VI)(aq) in bulk cloud and aerosol liquid water. These reactions are the dominant S(VI)(aq) reactions in cloud water at low and high pH, respectively [e.g., *Hoffmann and Calvert*, 1985; *Walcek and Taylor*, 1986; *Hegg et al.*, 1989; *Barth et al.*, 1992; *Mari et al.*, 2000]. In fact, over

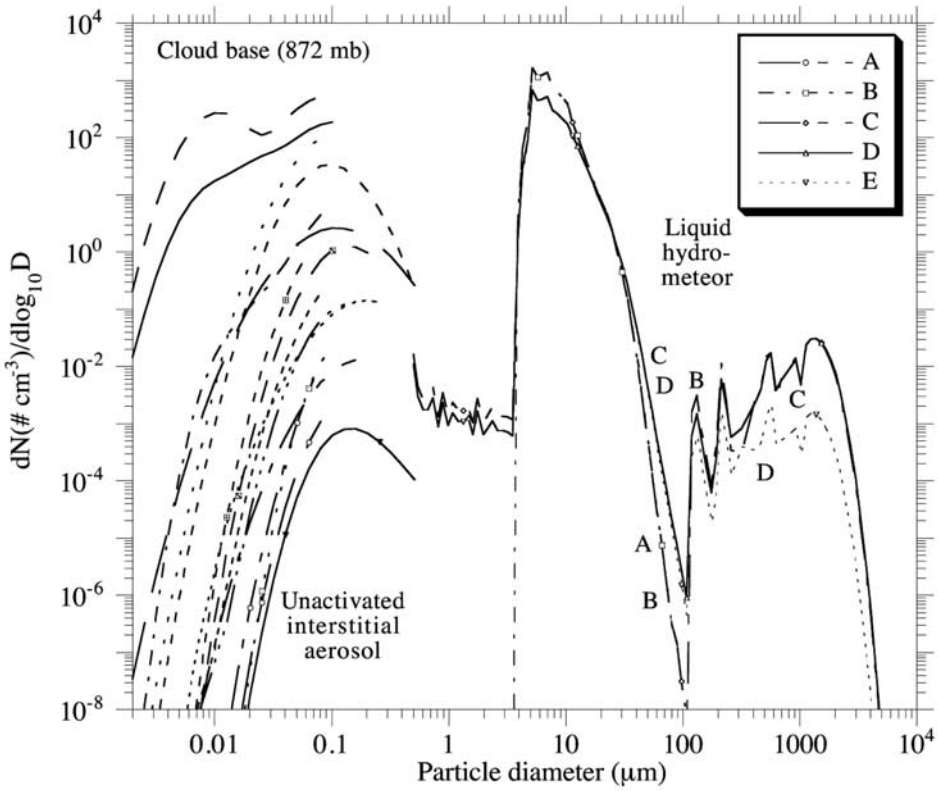

Figure 14. The left side shows unactivated aerosols at 872 mb (cloud base) from the one-dimensional simulation after a 1-hour growth time step. The right side shows the evolution of the liquid hydrometeor distribution at the end of an operator-split 1-hour time step of (a) condensation, (b) condensation plus settling from above, (c) coagulation of condensed and settled hydrometeors, and (d) sedimentation (for a half-step) of coagulated hydrometeors. The legend and initial conditions for aerosol distributions are given in Figure 3.

a range of liquid water contents (0.0003–9 g m^{-3}), pH values (0–8), and temperatures, these reactions may be the major sinks of SO_2(g) in aerosols and clouds [*Liang and Jacobson*, 1999]. Overall reaction rates for the two reactions are a combination of an effective Henry's constant for each reactant, aqueous reaction rates for intermediate reactions, and liquid water content, summed over all hydrometeor and aerosol sizes. Cloud water is obtained from the half point of the settling calculation. The bulk S(VI)(aq) produced from the two reactions is distributed over each cloud and aerosol size bin proportionately to liquid water volume in the bin. The incremental S(VI)(aq) assigned to each bin is added to the S(VI)(aq) already in the bin.

5. Analysis of Cloud Interactions With Multiple Aerosol Distributions

[68] Here the cloud module is analyzed in a one-dimensional simulation, introduced in section 2. During the simulation, a cumulonimbus cloud with base at 872 mb and top near 90 mb, evolved. The cloud contained liquid, mixed-phase, and ice sectors. All processes described in sections 3 and 4 were treated. The equilibrium cumulus and stratus parameterizations were used to obtain first guesses of cloud water and thermodynamic variables. Remaining processes were solved over a 1-hour time step (h = 3600 s).

5.1. Effect of Solute and Surface Tension on Activation

[69] Following evaporation of bulk water (section 3.4), clouds and precipitation were formed on the 16 aerosol distributions in Figure 3, with vertical variation as in Figure 2. The left side of Figure 14 shows the unactivated (interstitial) aerosols after the 1-hour time step of condensation at cloud base (872 mb). Aerosol activation diameters were smallest for particles containing electrolyte solutions or OM (sea spray, sulfate, OM, spray-sulfate, spray-OM, sulfate-OM), largest for particles containing neither (soil, BC, soil-BC), and in-between for distributions containing some electrolytes or OM (spray-soil, spray-BC, soil-sulfate, soil-OM, sulfate-BC, BC-OM). The presence of dissolved solutes decreased critical supersaturations (equation (10)). Dissolved solutes and OM decreased surface tensions, further decreasing critical supersaturations. In both cases, reduced supersaturations increased activation (even though the critical radius increased in both cases, equation (10)) in comparison with when a dilute water surface was assumed. The results here support numerous studies that have found that solute and surface tension affect the activation size of cloud drops. Because externally mixed soot contained no solute, it activated at larger size than did externally mixed sulfate. This suggests that the first indirect climate effect of soot on clouds may be less than that of sulfate, which was found by *Jacobson* [2002a] with the module described here.

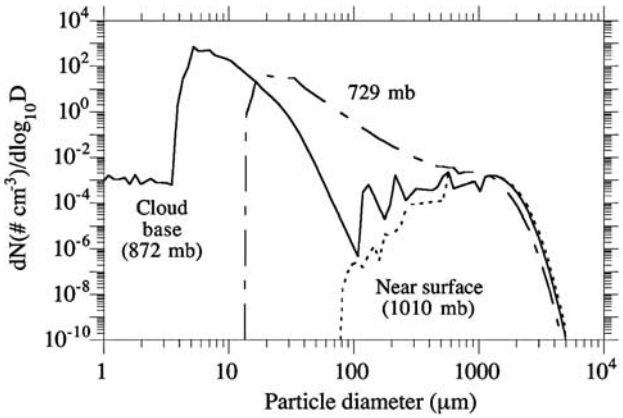

Figure 15. Baseline-case hydrometeor distributions after the first sedimentation half time step in three model layers in the one-dimensional simulation.

5.2. Effect of HHC on Clouds

[70] Curve a on the right side of Figure 14 is the liquid hydrometeor distribution after condensation onto activated CCN. This is the same distribution as the 872-mb distribution shown in Figure 5a. Curve b in Figure 14 is curve a plus the distribution of hydrometeors settled from the layer above. The curve indicates that the two major modes of hydrometeors in the layer were due to growth of new drops on activated CCN and settling from above. The particles smaller than 4 μm diameter at cloud base were aerosol cores or partially grown hydrometeors that settled from above. Curve c shows the effect of a 1-hour HHC step applied to curve b. Coagulation reduced the peak number concentration of the growth mode and shifted the mode to larger sizes. Coagulation of growth-mode particles with the sedimentation mode also shifted smaller sedimentation-mode particles to slightly larger sizes. In this simulation, coagulation did not produce liquid drops large enough to break up (a case with breakup is shown shortly). Curve d shows the effect on Curve c of a half time step of settling to below. A half step of settling was shown since the resulting concentration is that used for aerosol-hydrometeor coagulation and aqueous chemistry. Settling removed primarily large particles.

[71] Figure 15 compares liquid distributions at two levels in the cloud and at the surface after the first sedimentation half time step. The distribution at 729 mb had a larger mean radius for the condensation mode than that at cloud base, as explained previously with respect to Figure 5. All three distributions had precipitation modes. Near the ground, drops primarily >100 μm diameter survived since smaller drops did not have sufficient fall speed to reach this level during the 1-hour time step or they evaporated prior to reaching it.

[72] Figure 16a compares curve d from Figure 14 with that from a case in which HHC was ignored in all layers of the model. When coagulation was ignored, the second mode of hydrometeors shown in Figure 16a was due to sedimentation from large ice particles that settled and melted from layers above and from large liquid condensation drops settling from above (Figure 5). Neglecting coagulation prevented the growth of large precipitation drops, as expected.

[73] Figure 16b shows results at cloud base from three additional simulations in which HHC was faster ($x = 0$ in equation (29)) than in the baseline case ($x = 1/3$). The three cases include one with only $x = 0$, one with $x = 0$ and no drop breakup, and one with $x = 0$ and with drop breakup after the half step of sedimentation instead of before it. In these simulations, HHC produced particles sufficiently large to be broken up, as illustrated in the "no breakup" case. Without breakup, almost all particles 0.2–6 mm were eliminated. With breakup ("baseline"), huge particles were redistributed to smaller sizes, forming the second mode. When breakup was solved after instead of before a half step of sedimentation, the second mode was slightly smaller since sedimentation removed the largest drops before they could be broken up.

[74] In sum, concentrations of liquid drops 0.1–5 mm diameter were affected by HHC and breakup. When coagulation was slow, drops entered this size region but did not become much larger. When coagulation was fast, drops passed through this region quickly, but were redistributed by breakup back into it.

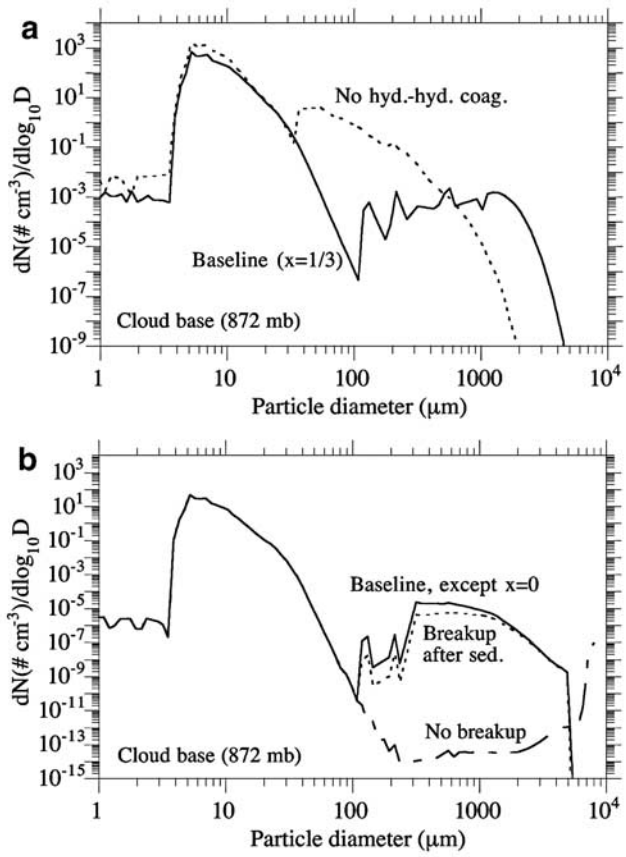

Figure 16. (a) Comparison of the liquid hydrometeor distribution at cloud base from the baseline case ($x = 1/3$ in equation (29)) with that from a sensitivity simulation in which no hydrometeor-hydrometeor coagulation was included. (b) Comparison of three sensitivity simulations, where $x = 0$ in all cases. The three cases include a baseline case, a case without drop breakup, and a case with drop breakup after the half-step of sedimentation instead of before it.

5.3. Effect of Aerosol-Hydrometeor Coagulation on Aerosol Removal

[75] Aerosol number removal is due to four processes: rainout (nucleation scavenging), washout (impaction scavenging), sedimentation, and dry deposition (evaporation and chemistry do not reduce aerosol number). Rainout is due to condensation and deposition of water onto CCN and IDN, respectively, followed by removal of the hydrometeor. Washout is due to coagulation of hydrometeors with interstitial aerosols, followed by removal of the hydrometeors. Neither aerosol sedimentation nor dry deposition were included in the simulation here to isolate the effects of rainout and washout.

[76] In the baseline case, approximately 32% of initial aerosol particles by number were activated within the cloud. This number is lower than that from some studies of cloud nucleation that have predicted activation rates of 50% or more [e.g., *Flossmann et al.*, 1985]. One reason for the difference is that all studies to date have assumed activation onto a single soluble aerosol distribution. Here 16 distributions were treated, some with low solubility (Figure 14). A second reason is that the aerosol distributions here were trimodal, including a nucleation mode. Studies that do not include the nucleation mode will predict greater activation fractions because the nucleation mode contains the greatest particle number, and most of these particles are not activated. When the module described in this paper was applied to a case consisting of a single lognormal ammonium sulfate distribution, 50% of the particles were activated [*Kreidenweis et al.*, 2003].

[77] Given that rainout removed about 32% of in-cloud aerosol number, remaining in-cloud removal and all below-cloud removal must have been due to washout. To check the magnitude of rainout versus washout, a simulation was run in which aerosol-hydrometeor coagulation was turned off. Figure 2 compares weighted-average clear-sky plus cloudy-sky results from this sensitivity with results from the baseline case. The difference between the "...with aer.-hyd. coag" and the "...no-aer.-hyd. coag." curves is the relative effect of washout (aerosol-hydrometeor coagulation) on aerosol removal. The difference between the "...no-aer.-hyd. coag." and the "after convection, before physics" curves is the effect of rainout on removal. The result suggests that, within the cloud, washout removed 42% of particles by number, more than rainout did (32%). In terms of mass, though, rainout removed about 60%, washout removed <0.1%. Because rainout scavenged all large and most midsize particles, which have large masses, washout could remove only smaller particles, which were more numerous but less massive. The results here are consistent with those of *Kreidenweis et al.* [1997] who found that washout removed $\ll$1% of S(VI) mass within a cloud (they did not look at number).

[78] Within plus below the cloud, washout removed 44% of particle number, whereas rainout removed 14%. Below the cloud, washout was the only mechanism of aerosol removal. Figure 17a compares the summed aerosol distribution in the layer immediately below cloud base before and after cloud microphysics. In this layer, washout removed about 60% of particle number and 62% of mass. Within the cloud, washout had little effect on mass because rainout removed most mass. Below the cloud, rainout did not operate, so washout could remove large and small particles, affecting mass and number. In the layer adjacent to the ground, washout removed only 5.4% of particles by number and 5.8% by mass. A reason for the decrease in removal with decreasing height is that midsize precipitation drops evapo-

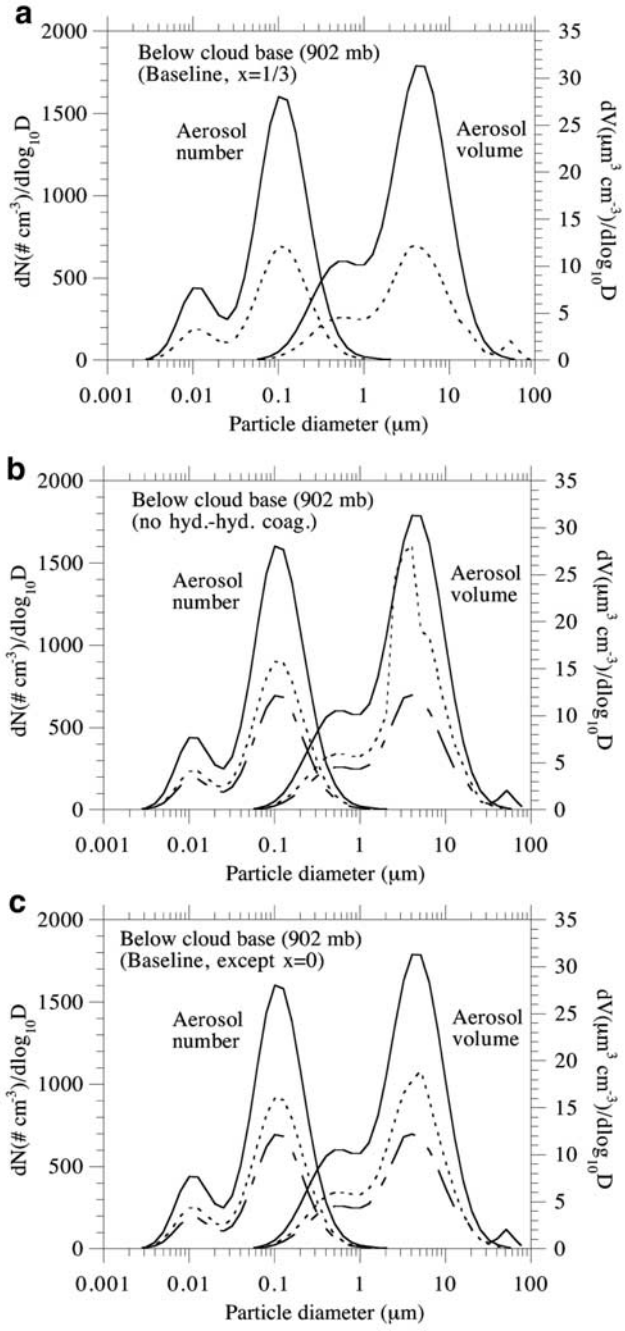

Figure 17. (a) Below cloud base aerosol number and volume, summed over 16 size distributions, before (solid lines) and after (short-dashed lines) cloud microphysics. The "before" curves were obtained after cumulus convection, so the plot shows the effect on aerosol scavenging of cloud microphysics only. (b) Same as Figure 17a, but with no hydrometeor-hydrometeor coagulation. The base-case "after" curve is also shown for comparison (long-dashed lines). (c) Same as Figure 17a, but when $x = 0$ instead of $x = 1/3$ in equation (29) and also with the base-case "after" curve for comparison (long-dashed lines).

rated and larger ones shrank between below cloud base and the ground reducing aerosol-hydrometeor coagulation rates.

[79] Of the total column-integrated mass loss of SO_2 + particulate sulfate, about 11% was due to aerosol-hydrometeor coagulation (washout). The rest was due to the combination of aerosol rainout (nucleation scavenging of initial sulfate particles) and gas washout (dissolution and aqueous chemistry of SO_2 followed by removal). This result is in the range of that of *Hegg et al.* [1984], who found that, of all SO_2 + particulate sulfate mass removed from two types of clouds, 8–57% was due to below-cloud washout.

[80] Given that rainout removes only large particles, that washout is the dominant below-cloud removal mechanism, and that particle loadings are highest below clouds, the results here suggest that washout must be a more-important in-plus-below-cloud removal process than rainout in terms of aerosol number. The opposite is true for aerosol mass.

5.4. Effect of HHC on Aerosol Removal

[81] Figure 17b shows the effect of ignoring HHC on below-cloud aerosol removal. Without HHC, large hydrometeors from layers above penetrated below the cloud (Figure 16a), collecting and removing some aerosols (Figure 17b). Overall, though, fewer aerosols, particularly large ones, were removed when HHC was ignored than in the baseline case (Figure 17a). Also, fewer large than small aerosols were removed because many hydrometeors that settled below the cloud evaporated there, releasing mostly large aerosol cores, offsetting the washout of other large aerosols.

[82] When HHC rates were greater than in the baseline case ($x = 0$, Figure 17c), below-cloud aerosol removal rates were also lower than in the baseline case ($x = 1/3$). Fast HHC rates produced fewer but larger hydrometeors than did slow HHC rates. Larger hydrometeors fell through the subcloud layer faster than did smaller ones. In addition, fewer, larger drops had smaller total cross-sectional areas than did more, smaller drops. Both factors contributed to lower washout rates in Figure 17c than in Figure 17a.

[83] In sum, when HHC rates are slow, hydrometeors are small and may evaporate/sublimate before washing out aerosols. When HHC rates are fast, hydrometeors are heavy and fall fast, reducing washout rates as well. Washout rates are maximized when HHC rates are between the two extremes. Since HHC affects washout substantially, and washout appears to be the major removal mechanism of aerosol number in clouds (section 5.3), and wet deposition appears to be the most effective method of aerosol removal in the atmosphere [e.g., *Langner and Rodhe*, 1991; *Pham et al.*, 1995], HHC appears to have a substantial effect on aerosol number globally. Since the quantity of aerosols determines the quantity of hydrometeors, and therefore HHC rates, aerosol emission can feed back to aerosol removal through the effect of emission on HHC. Some model uncertainties in the magnitude of this feedback include uncertainties in coagulation rates, aerosol emission rates, cloud lifetime, cloud height, and cloud turbulence, among others.

5.5. Effect of Freezing on Aerosol Removal

[84] Two final tests were run to examine the effect of HHF and CF on clouds and aerosol removal. For the simulations, HHF and CF, respectively, were shut off. Figure 18 shows the difference in liquid and graupel distributions in the layer below cloud top from the HHF removal case. The figure shows that treating HHF (baseline case) converted primarily large liquid drops to graupel. However, since graupel already existed from other processes in precipitation-mode drops, the major addition of HHF was to increase graupel particles in the 50–300 μm range. Yet graupel in this size range, like the liquid drops they replaced, tended to sublimate before they could fall or coagulate with other hydrometeors sufficiently. As a result, the removal of HHF had virtually no effect on the hydrometeor distribution in all-liquid layers, such as at 729 mb. Further, it had virtually no impact on aerosol removal in liquid layers or below cloud base.

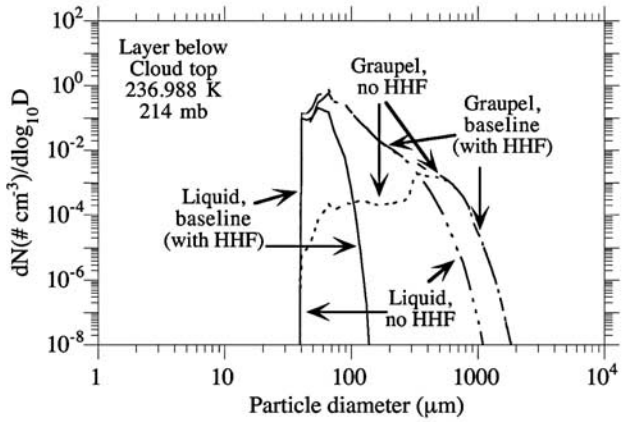

Figure 18. Comparison of liquid and graupel distributions in the layer below cloud top from the baseline case with those from a case with no HHF. The temperature is the in-cloud temperature.

[85] Whereas HHF freezes primarily large liquid drops, CF freezes a higher proportion of small drops since these are more likely to coagulate with aerosol particles. Although the coagulation rate coefficient of an aerosol particle with a hydrometeor generally increases with increasing size, the number concentration of large particles decreases with size at a greater rate, causing the aerosol-hydrometeor coagulation rate to decrease with increasing size. Even though CF froze primarily small drops, the number of aerosol particles in the upper troposphere was sufficiently small that CF had relatively little effect on the size distribution of liquid or graupel in mixed-phase layers. Even when all aerosol particles were assumed to freeze a drop upon contact, the effect was still small. As such, under upper-tropospheric conditions, it appears that HHF is a more important mechanism of drop freezing than is CF. In cold, lower-tropospheric regions in which aerosol particle concentrations are high (e.g., in populated Northern latitude regions during winter), it is likely that CF is a more important freezing mechanism.

6. Conclusions

[86] In this paper, numerical techniques were developed to simulate the evolution of clouds and precipitation from multiple aerosol size distributions and the effect of clouds

and precipitation on aerosol removal. Techniques developed include those for (1) growth of liquid and ice clouds onto multiple aerosol size distributions; (2) coagulation of liquid and ice and their aerosol components to form size-resolved graupel, and larger liquid and ice hydrometeors using a kernel that accounts for diffusiophoresis, thermophoresis, electric charge, gravitation, Brownian motion, diffusion enhancement, turbulent shear, and turbulent inertia; (3) Contact freezing of size-resolved liquid by coagulation with interstitial aerosols; (4) size-resolved heterogeneous plus homogeneous freezing; (5) large liquid drop breakup; (6) coagulation of cloud hydrometeors and incorporated aerosols with interstitial aerosols; (7) coagulation of precipitation with interstitial and below-cloud aerosols (washout); (8) removal of precipitation and incorporated aerosols (rainout); (9) below- and in-cloud shrinkage of precipitation to smaller drops and aerosol cores; (10) gas washout; and (11) aqueous cloud and aerosol chemistry.

[87] Findings of the study include the following: (1) hydrometeor-hydrometeor coagulation appears to play a substantial role in controlling aerosol-particle number globally; (2) washout (aerosol-hydrometeor coagulation) may be a more important in-plus below-cloud removal mechanism of aerosol number than rainout (the opposite is true for aerosol mass, a result consistent with that from studies that have looked at mass); (3) close-in diameter dual peaks in observed cloud distributions may be in part due to different activation characteristics of different aerosol distributions; (4) evaporative cooling at liquid drop surfaces in subsaturated air may be a mechanism of drop freezing (referred to here as ''evaporative freezing''); cooling rates are greater in the lower than upper troposphere; this theory needs to be tested experimentally; and (5) heterogeneous-homogeneous freezing may freeze more upper-tropospheric drops than contact freezing, but neither appears to affect warm-cloud hydrometeor distributions or aerosol scavenging substantially.

[88] **Acknowledgments.** I would like to thank Amy Stuart and Azadeh Tabazadeh for helpful comments. This work was supported by the NASA New Investigator Program in Earth Sciences, the Environmental Protection Agency Office of Air Quality Planning and Standards, and the National Science Foundation Atmospheric Chemistry Division.

References

Ackerman, A. S., O. B. Toon, and P. V. Hobbs, A model for particle microphysics, turbulent mixing, and radiative transfer in the stratocumulus-topped marine boundary layer and comparisons with measurements, *J. Atmos. Sci.*, *52*, 1204–1236, 1995.

Arakawa, A., and V. R. Lamb, Computational design of the basic dynamical processes of the UCLA general circulation model, *Methods Comput. Phys.*, *17*, 174–265, 1977.

Arakawa, A., and W. H. Schubert, Interaction of cumulus cloud ensemble with the large-scale environment, part I, *J. Atmos. Sci.*, *31*, 674–701, 1974.

Barth, M. C., D. A. Hegg, and P. V. Hobbs, Numerical modeling of cloud and precipitation chemistry associated with two rainbands and some comparisons with observations, *J. Geophys. Res.*, *97*, 5825–5845, 1992.

Barth, M. C., A. L. Stuart, and W. C. Skamarock, Numerical simulations of the July 10 stratospheric-tropospheric experiment: Radiation, aerosols, and ozone/deep convection storm: Redistribution of soluble tracers, *J. Geophys. Res.*, *106*, 12,381–12,400, 2001.

Beard, K. V., Terminal velocity and shape of cloud and precipitation drops aloft, *J. Atmos. Sci.*, *33*, 851–864, 1976.

Beard, K. V., and S. N. Grover, Numerical collision efficiencies for small raindrops colliding with micron size particles, *J. Atmos. Sci.*, *31*, 543–550, 1974.

Beard, K. V., and H. T. Ochs III, Collection and coalescence efficiencies for accretion, *J. Geophys. Res.*, *89*, 7165–7169, 1984.

Beard, K. V., and H. R. Pruppacher, A wind tunnel investigation of the rate of evaporation of small water drops falling at terminal velocity in air, *J. Atmos. Sci.*, *28*, 1455–1464, 1971.

Betts, A. K., and M. J. Miller, A new convective adjustment scheme, part II, Single column tests using GATE wave, BOMEX, ATEX, and Arctic airmass data, *Q. J. R. Meteorol. Soc.*, *112*, 693–709, 1986.

Bigg, E. K., The formation of atmospheric ice crystals by the freezing of droplets, *Q. J. R. Meteorol. Soc.*, *79*, 510–519, 1953.

Bott, A., A flux method for the numerical solution of the stochastic collection equation: Extension to two-dimensional particle distributions, *J. Atmos. Sci.*, *57*, 284–294, 2000.

Boucher, O., and U. Lohmann, The sulfate-CCN-cloud albedo effect, *Tellus, Ser. B*, *47*, 281–300, 1995.

Chen, J.-P., and D. Lamb, Simulation of cloud microphysical and chemical processes using a multicomponent framework, part I, Description of the microphysical model, *J. Atmos. Sci.*, *51*, 2613–2630, 1994.

Chen, J.-P., and D. Lamb, Simulation of cloud microphysical and chemical processes using a multicomponent framework, part II, Microphysical evolution of a wintertime orographic cloud, *J. Atmos. Sci.*, *56*, 2293–2312, 1999.

Chuang, C. C., and J. E. Penner, Effects of anthropogenic sulfate on cloud drop nucleation and optical properties, *Tellus, Ser. B*, *47*, 566–577, 1995.

Danielsen, E. F., R. Bleck, and D. A Morris, Hail growth by stochastic collection in a cumulus model, *J. Atmos. Sci.*, *29*, 135–155, 1972.

Ding, P., and D. A. Randall, A cumulus parameterization with multiple cloud base levels, *J. Geophys. Res.*, *103*, 11,341–11,353, 1998.

Facchini, M. C., M. Mircea, S. Fuzzi, and R. J. Charlson, Cloud albedo enhancement by surface-active organic solutes in growing droplets, *Nature*, *401*, 257–259, 1999.

Feingold, G., S. M. Kreidenweis, B. Stevens, and W. R. Cotton, Numerical simulations of stratocumulus processing of cloud condensation nuclei through collision-coalescence, *J. Geophys. Res.*, *101*, 21,391–21,402, 1996.

Feingold, G., S. M. Kreidenweis, and Y. Zhang, Stratocumulus processing of gases and cloud condensation nuclei, 1, Trajectory ensemble model, *J. Geophys. Res.*, *103*, 19,527–19,542, 1998.

Ferrier, B. S., A double-moment multiple-phase four-class bulk ice scheme, part I, Description, *J. Atmos. Sci.*, *51*, 249–280, 1994.

Flossmann, A. I., W. D. Hall, and H. R. Pruppacher, A theoretical study of the wet removal of atmospheric pollutants, part I, The redistribution of aerosol particles captured through nucleation and impaction scavenging by growing cloud drops, *J. Atmos. Sci.*, *42*, 582–606, 1985.

Fowler, L. D., D. A. Randall, and S. A. Rutledge, Liquid and cloud ice microphysics in the CSU GCM, part I, Model description and simulated microphysical processes, *J. Clim.*, *9*, 489–529, 1996.

Fuchs, N. A., *The Mechanics of Aerosols*, translated by R. E. Daisley and M. Fuchs, Pergamon, New York, 1964.

Ghan, S., R. Easter, J. Hudson, and F.-M. Breon, Evaluation of aerosol indirect radiative forcing in MIRAGE, *J. Geophys. Res.*, *106*, 5317–5334, 2001.

Grell, G. A., Y.-H. Kuo, and R. J. Pasch, Semiprognostic tests of cumulus parameterization schemes in middle latitutdes, *Mon. Weather Rev.*, *119*, 5–31, 1991.

Guriciullo, C. S., and S. N. Pandis, Effect of composition variations in cloud droplet populations on aqueous chemistry, *J. Geophys. Res.*, *102*, 9375–9385, 1997.

Hall, W. D., A detailed microphysical model within a two-dimensional dynamic framework: Model description and preliminary results, *J. Atmos. Sci.*, *37*, 2486–2507, 1980.

Hegg, D. A., S. A. Rutledge, and P. V. Hobbs, A numerical model for sulfur chemistry in warm-frontal rainbands, *J. Geophys. Res.*, *89*, 7133–7147, 1984.

Hegg, D. A., S. A. Rutledge, P. V. Hobbs, M. C. Barth, and O. Hertzman, The chemistry of a mesoscale rainband, *Q. J. R. Meteorol. Soc.*, *115*, 867–886, 1989.

Hoffmann, M. R., and J. G. Calvert, Chemical transformation modules for Eulerian acid deposition modules, vol. 2, The aqueous-phase chemistry (EPA/600/3-85/017), U.S. Environ. Prot. Agency, Research Triangle Park, N. C., 1985.

Hounslow, M. J., R. L. Ryall, and V. R. Marshall, A discretized population balance for nucleation, growth, and aggregation, *AIChE J.*, *34*, 1821–1832, 1988.

Jacobson, M. Z., Development and application of a new air pollution modeling system, part II, Aerosol module structure and design, *Atmos. Environ.*, *31*, 131–144, 1997a.

Jacobson, M. Z., Numerical techniques to solve condensational and dissolutional growth equations when growth is coupled to reversible reactions, *Aerosol Sci. Technol.*, *27*, 491–498, 1997b.

Jacobson, M. Z., *Fundamentals of Atmospheric Modeling*, Cambridge Univ. Press, New York, 1999.

Jacobson, M. Z., GATOR-GCMM: A global through urban scale air pollution and weather forecast model, 1, Model design and treatment of subgrid soil, vegetation, roads, rooftops, water, sea ice, and snow, *J. Geophys. Res.*, *106*, 5385–5402, 2001.

Jacobson, M. Z., Control of fossil-fuel particulate black carbon plus organic matter, possibly the most effective method of slowing global warming, *J. Geophys. Res.*, *107*(D19), 4410, 10.1029/2001JD001376, 2002a.

Jacobson, M. Z., Analysis of aerosol interactions with numerical techniques for solving coagulation, nucleation, condensation, dissolution, and reversible chemistry among multiple size distributions, *J. Geophys. Res.*, *107*(D19), 4366, 10.1029/2001JD002044, 2002b.

Jacobson, M. Z., R. P. Turco, E. J. Jensen, and O. B. Toon, Modeling coagulation among particles of different composition and size, *Atmos. Environ. Part A*, *28*, 1327–1338, 1994.

Jones, A., D. L. Roberts, M. J. Woodage, and C. E. Johnson, Indirect sulphate aerosol forcing in a climate model with an interactive sulphur cycle, *J. Geophys. Res.*, *106*, 20,293–20,310, 2001.

Kogan, Y. L., The simulation of a convective cloud in a 3-D model with explicit microphysics, part I, Model description and sensitivity experiments, *J. Atmos. Sci.*, *48*, 1160–1189, 1991.

Kogan, Z. N., Y. L. Kogan, and D. K. Lilly, Cloud factor and seasonality of the indirect effect of anthropogenic sulfate aerosols, *J. Geophys. Res.*, *102*, 25,927–25,939, 1997.

Kreidenweis, S. M., Y. Zhang, and G. R. Taylor, The effects of clouds on aerosol and chemical species production and distribution, 2, Chemistry model description and sensitivity analysis, *J. Geophys. Res.*, *102*, 23,867–23,882, 1997.

Kreidenweis S. M., C. Walcek, C.-H. Kim, G. Feingold, W. Gong, M. Z. Jacobson, X. Liu, J. Penner, A. Nenes, and J. H. Seinfeld, Modification of aerosol mass and size distribution due to aqueous-phase SO_2 oxidation in clouds: Comparison of several models, *J. Geophys. Res.*, *108*(D7), 4213, doi:10.1029/2002JD002697, 2003.

Kuo, H. L., Further studies of the parameterization of the influence of cumulus convection on largescale flow, *J. Atmos. Sci.*, *31*, 1232–1240, 1974.

Langner, J., and H. Rodhe, A global three-dimensional model of the tropospheric sulfur cycle, *J. Atmos. Chem.*, *13*, 225–263, 1991.

Lee, I. Y., Comparison of cloud microphysics parameterizations for simulation of mesoscale clouds and precipitation, *Atmos. Environ. Part A*, *26*, 2699–2712, 1992.

Lee, I. Y., and H. M. Park, Comparison of microphysics parameterizations in a three-dimensional dynamic cloud model, *Atmos. Environ.*, *28*, 1615–1625, 1994.

Li, Z., A. L. Williams, and M. J. Rood, Influence of soluble surfactant properties on the activation of aerosol particles containing inorganic solute, *J. Atmos. Sci.*, *55*, 1859–1866, 1998.

Liang, J., and M. Z. Jacobson, A study of sulfur dioxide oxidation pathways over a range of liquid water contents, pH values, and temperatures, *J. Geophys. Res.*, *104*, 13,749–13,769, 1999.

List, R., and J. R. Gillespie, Evolution of raindrop spectra with collision-induced breakup, *J. Atmos. Sci.*, *33*, 2007–2013, 1976.

Lister, J. D., D. J. Smit, and M. J. Hounslow, Adjustable discretized population balance for growth and aggregation, *AIChE J.*, *41*, 591–603, 1995.

Liu, X., and W. Seidl, Modeling study of cloud droplet nucleation and in-cloud sulfate production during the sanitation of the atmosphere (SANA) 2 campaign, *J. Geophys. Res.*, *103*, 16,145–16,158, 1998.

Lohmann, U., Possible aerosol effects on ice clouds via contact nucleation, *J. Atmos. Sci.*, *59*, 647–656, 2002.

Lohmann, U., J. Feichter, J. Penner, and R. Leaitch, Indirect effect of sulfate and carbonaceous aerosols: A mechanistic treatment, *J. Geophys. Res.*, *105*, 12,193–12,206, 2000.

Lu, R., and R. P. Turco, Air pollutant transport in a coastal environment, part I, Two-dimensional simulations of sea-breeze and mountain effects, *J. Atmos. Sci.*, *51*, 2285–2308, 1994.

Manabe, S., and J. L. Holloway Jr., Simulation of climate by a global general circulation model. Hydrologic cycle and heat balance, *Mon. Weather Rev.*, *99*, 335–369, 1971.

Mari, C., D. J. Jacob, and P. Bechtold, Transport and scavenging of soluble gases in a deep convective cloud, *J. Geophys. Res.*, *105*, 22,255–22,267, 2000.

Martin, J. J., P. K. Wang, and H. R. Pruppacher, A theoretical study of the effect of electric charges on the efficiency with which aerosol particles are collected by ice crystal plates, *J. Colloid Interface Sci.*, *78*, 44–56, 1980.

Mellor, G. L., and T. Yamada, Development of a turbulence closure model for geophysical fluid problems, *Rev. Geophys. Space Phys.*, *20*, 851–875, 1982.

Menon, S., A. D. Del Genio, D. Koch, and G. Tselioudis, GCM simulations of the aerosol indirect effect: Sensitivity to cloud parameterization and aerosol burden, *J. Atmos. Sci.*, *59*, 692–713, 2002.

Meyers, M. P., P. J. DeMott, and W. R. Cotton, New primary ice-nucleation parameterization in an explicit cloud model, *J. Appl. Meteorol.*, *31*, 708–721, 1992.

Mordy, W., Computations of the growth by condensation of a population of cloud droplets, *Tellus*, *11*, 16–44, 1959.

Orville, H. D., and F. J. Kopp, Numerical simulations of the history of a hailstorm, *J. Atmos. Sci.*, *34*, 1596–1618, 1977.

Ovtchinnikov, M., and Y. L. Kogan, An investigation of ice production mechanisms in small cumuliform clouds, using a 3D model with explicit microphysics, part I, Model description, *J. Atmos. Sci.*, *57*, 2989–3003, 2000.

Pham, M., J.-F. Muller, G. P. Brasseur, C. Granier, and G. Megie, A three-dimensional study of the tropospheric sulfur cycle, *J. Geophys. Res.*, *100*, 26,061–26,092, 1995.

Pitter, R. L., and H. R. Pruppacher, A wind tunnel investigation of freezing of small water drops falling at terminal velocity in air, *Q. J. R. Meterol. Soc.*, *99*, 540–550, 1973.

Pruppacher, H. R., and J. D. Klett, *Microphysics of Clouds and Precipitation*, 2nd ed., Kluwer Acad., Norwell, Mass., 1997.

Pruppacher, H. R., and R. Rasmussen, A wind tunnel investigation of the rate off evaporation of large water drops falling at terminal velocity in air, *J. Atmos. Sci.*, *36*, 1255–1260, 1979.

Rasmussen, R., and H. R. Pruppacher, A wind tunnel and theoretical study of the melting behavior of atmospheric ice particles, part I, A wind tunnel study of frozen drops of radius <500 mm, *J. Atmos. Sci.*, *39*, 152–158, 1982.

Rasmussen, R., M. V. Levizzani, and H. R. Pruppacher, A wind tunnel and theoretical study of the melting behavior of atmospheric ice particles, part II, A theoretical study for frozen drops of radius <500 mm, *J. Atmos. Sci.*, *41*, 374–380, 1984.

Reisin, T., Z. Levin, and S. Tzivion, Rain production in convective clouds as simulated in an axisymmetric model with detailed microphysics, part I, Description of the model, *J. Atmos. Sci.*, *53*, 497–519, 1996.

Rotstayn, L. D., and J. E. Penner, Indirect aerosol forcing, quasi forcing, and climate response, *J. Clim.*, *14*, 2960–2975, 2001.

Slingo, J., The development and verification of a cloud prediction scheme for the ECMW model, *Q. J. R. Meteorol. Soc.*, *113*, 899–927, 1987.

Stuart, A. L., Volatile chemical partitioning during cloud hydrometeor freezing and its effects on tropospheric chemical distributions, Ph.D. thesis, Stanford Univ., Calif., 2002.

Sud, Y. C., and G. K. Walker, Microphysics of clouds with the relaxed Arakawa-Schubert scheme (McRAS), part I, Design and evaluation with GATE phase III data, *J. Atmos. Sci.*, *56*, 3196–3220, 1999.

Sundqvist, H., A parameterization of non-convective condensation including prediction of cloud water content, *Q. J. R. Meteorol. Soc.*, *104*, 677–690, 1978.

Tabazadeh, A., Y. S. Djikaev, and H. Reiss, Surface crystallization of supercooled water in clouds, *Proc. Natl. Acad. Sci. U.S.A.*, in press, 2003.

Tang, I., Thermodynamic and optical properties of mixed-salt aerosols of atmospheric importance, *J. Geophys. Res.*, *102*, 1883–1893, 1997.

Taylor, G. R., S. Kreidenweis, and Y. Zhang, The effects of clouds on aerosol and chemical species production and distribution, 1, Cloud model formulation, mixing, and detrainment, *J. Geophys. Res.*, *102*, 23,851–23,865, 1997.

Tiedtke, M., Representation of clouds in large-scale models, *Mon. Weather Rev.*, *121*, 3040–3061, 1993.

Turco, R. P., O. B. Toon, R. C. Whitten, R. G. Keesee, and D. Hollenbach, Noctilucent clouds: Simulation studies of their genesis, properties and global influences, *Planet. Space Sci.*, *30*, 1147–1181, 1982.

Tzivion, S., G. Feingold, and Z. Levin, An efficient numerical solution to the stochastic collection equation, *J. Atmos. Sci.*, *44*, 3139–3149, 1987.

Tzivion, S., G. Feingold, and Z. Levin, The evolution of raindrop spectra, part II, Collisional collection/breakup and evaporation in a rainshaft, *J. Atmos. Sci.*, *46*, 3312–3327, 1989.

Tzivion, S., T. Reisin, and Z. Levin, Numerical simulation of hygroscopic seeding in a convective cloud, *J. Appl. Meteorol.*, *33*, 252–267, 1994.

Vali, G., Quantitative evaluation of experimental results on the heterogeneous freezing nucleation of supercooled liquids, *J. Atmos. Sci.*, *28*, 402–409, 1971.

Walcek, C. J., and G. R. Taylor, A theoretical method for computing vertical distributions of acidity and sulfate production within cumulus clouds, *J. Atmos. Sci.*, *43*, 339–355, 1986.

Walko, R. L., W. R. Cotton, M. P. Meyers, and J. Y. Harrington, New RAMS cloud microphysics parameterization, part I, The single-moment scheme, *Atmos. Res.*, *38*, 29–62, 1995.

Wang, C., and J. S. Chang, A three-dimensional numerical model of cloud dynamics, microphysics, and chemistry, 1, Concepts and formulation, *J. Geophys. Res.*, *98*, 14,827–14,844, 1993.

Wang, P. K., S. N. Grover, and H. R. Pruppacher, On the effect of electric charges on the scavenging of aerosol particles by clouds and small raindrops, *J. Atmos. Sci.*, *35*, 1735–1743, 1978.

Wang, S., Defining marine boundary layer clouds with a prognostic scheme, *Mon. Weather Rev.*, *124*, 1817–1833, 1996.

Xu, K.-M., and D. A. Randall, A semiempirical cloudiness parameterization for use in climate models, *J. Atmos. Sci.*, *53*, 3084–3102, 1996.

Zhang, Y., S. M. Kreidenweis, and G. Feingold, Stratocumulus processing of gases and cloud condensation nuclei, 2, Chemistry sensitivity analysis, *J. Geophys. Res.*, *104*, 16,061–16,080, 1999.

M. Z. Jacobson, Department of Civil and Environmental Engineering, Stanford University, Terman Engineering Center, Room M-13, Stanford, CA 94305-4020, USA. (jacobson@stanford.edu)